Surface water temperature observations and ice phenology estimations for 1.4 million lakes globally

Maartje C. Korver [a,*], Bernhard Lehner [a,*], Jeffrey A. Cardille [b,c], Laura Carrea [d]

[a] McGill University, Department of Geography, Montréal, QC H3A 0B9, Canada
[b] McGill University, Department of Natural Resource Sciences, Montréal, QC H3A 0B9, Canada
[c] McGill University, Bieler School of Environment, Montréal, QC H3A 0B9, Canada
[d] University of Reading, Department of Meteorology, Reading, UK

ARTICLE INFO

ABSTRACT

Water temperature and ice cover are critical characteristics of the ecological, biogeochemical, and physical functioning of a lake. Site-specific observations of temperature and ice, however, are not available for most lakes in the world. Yet this information is crucial to understanding the global role of lakes in the functioning of the bio- and hydrosphere. Here, we present the LakeTEMP dataset, referring to the ~1.4 million lakes globally of the HydroLAKES database with a surface area exceeding 0.1 km^2, and consisting of two subsets: (1) an observational dataset that contains lake surface water temperatures (LSWTs), derived from Landsat 8 thermal radiance observations between 2013 and 2021 extracted at the lake center points; and (2) a dataset with monthly and yearly LSWT summary statistics and predictions of average yearly ice cover durations, interpolated from the observational dataset using seasonal trendlines. All observations underwent extensive quality control and filtering, based on outlier detection, overlapping imagery removal, and the removal of observations taken from dry lake beds. Validation of the LSWT observations was carried out with in-situ data and yielded an R^2, RMSE and median of differences of 0.93, 1.71 °C and 0.42 °C, respectively. The global average yearly LSWT is 6.3 °C, assuming 0 °C during times of presumed ice cover, and 12.4 °C when only considering periods of open water. About 8% of all lakes never freeze, ~6% have short or sporadic freezing periods, and ~86% freeze every year, corresponding to an estimated proportion of global lake surface area of 23%, 20%, and 57%, respectively. The warmest lakes in the world (average temperatures of up to 36 °C) are all artificial lakes used in the power plant, mining, salt extraction, and aquaculture industries. LakeTEMP fills a crucial spatial data gap in large-scale limnological research, especially for the incorporation of small lakes and understudied geographies of remote regions. Moreover, easy linkage to other large-scale datasets that use the unique lake identifiers from HydroLAKES, most notably the LakeATLAS database (56 hydro-environmental variables for each lake including anthropogenic influences), allows to explore characteristics that may be correlated to or affected by LSWT and ice cover. The data are in an analysis-ready format and openly available at https://doi.org/10.6084/m9.figshare.23844660.

1. Introduction

The surface water temperature of a lake is a crucial factor that affects physical, ecological, and biogeochemical processes. It reflects the energy exchanges at the water-atmosphere interface (Edinger et al., 1968) and drives the distribution of heat throughout a lake's water column (Woolway et al., 2014). In addition, water temperature influences the metabolism, behavior, and the structure and dynamics of trophic networks (Woodward et al., 2010), the distribution of species (Sunday et al., 2012), in-lake chemical transformations (Vachon et al., 2021),

bottom-water anoxia (Jane et al., 2021), and greenhouse gas emissions (Jansen et al., 2022). Measurements of lake surface water temperature (LSWT) have long been gathered at individual lakes to inform local or regional water management practices and research programs. Monitoring of broad-scale geographic and temporal patterns of LSWT across very large numbers of lakes, however, has been much more challenging. Yet temperature is vital to understanding Earth's aquatic cycle (Downing, 2009). This includes exploring the role of lakes as sentinels of climate change (Adrian et al., 2009), as habitats of a global heritage of biodiversity (Heino et al., 2021), and as providers of diverse services to

humans (Janssen et al., 2021).

Lake ice, a physical property closely connected to LSWT, affects lake functioning most notably by creating a seal between the water-atmosphere interface, reducing the penetration of sunlight (Dombrovsky and Kokhanovsky, 2023), blocking turbulent fluxes such as greenhouse gasses (Striegl et al., 2001), and inducing reversed thermal stratification (Yang et al., 2021). On a global scale, the interactions of lake ice and climate are of special interest as the timing of freeze up and break up events (i.e., lake ice phenology) are sensitive indicators of air temperature changes (Marszelewski and Skowron, 2006), and the presence or lack of ice cover also influences regional climate and weather events by regulating the amount of evaporation (Zhao et al., 2022), thermal moderation, and lake-effect snow events (Balsamo et al., 2012; Brown and Duguay, 2010). In addition, freshwater ice provides cultural services (e.g., transport, recreation, spiritual values) that are especially important for Northern communities (Knoll et al., 2019).

Assembling a large-scale dataset of in-situ measurements of either LSWT or lake ice phenology requires extensive networking, collaboration, and data harmonization efforts. Impressive initiatives have addressed this challenge (e.g., Sharma et al., 2015; Sharma et al., 2022), but the resulting datasets remain limited with respect to the number of lakes included, their geographical and temporal coverage, and the consistency in data format and quality between sources. Remote sensing offers a solution to the latter two of these issues, as satellites can achieve nearly full coverage of the globe with consistent acquiring methods. However, the number of lakes contained in existing large-scale, satellite-derived datasets of LSWT and ice phenology are at present constrained to a few thousand lakes. These include datasets that are global but limited to large-sized lakes (Carrea et al., 2023; MacCallum and Merchant, 2012; Du and Kimball, 2018 for LSWT and Cai et al., 2021; Wang et al., 2022 for ice phenology), and datasets that are of higher spatial resolution but limited to the regional scale (e.g., Attiah et al., 2023; Giroux-Bougard et al., 2023). Studies have also estimated historical LSWTs with physical and machine learning models for ~90,000 lakes globally (Tong et al., 2023) and ~180,000 in the United States (Willard et al., 2022), but observational and comprehensive global LSWT or ice

phenology data are not available for over 95% of the millions of lakes in the world that are small or medium-sized (Messager et al., 2016; Pi et al., 2022). As a result, existing empirical knowledge of global lake thermal processes (e.g., Maberly et al., 2020; Woolway and Merchant, 2019) are typically based on large lakes only, yet heat exchanges across the water-atmosphere interface and the distribution of heat throughout the water column are size-dependent (Martinsen et al., 2019; Winslow et al., 2015; Woolway et al., 2017).

To address the described data and knowledge gaps, we assembled thermal data for all lakes between 84°N and 56°S that are at least 0.1 km^2 in surface area, as depicted in the HydroLAKES database (Messager et al., 2016). Observations were acquired from a small buffer around each lake's center location to minimize the accidental inclusion of land surfaces, and to ensure consistent comparisons across the dataset of ~1.4 million lakes. We used the Landsat 8 Earth Observation satellite (launched in April 2013) which carries a thermal infrared (TIR) sensor providing data at a resolution of 0.9 arc-seconds (30 m at the equator). With the dual band TIR sensor on board Landsat 8, surface temperature can be derived using a split-window (SW) algorithm, which dismisses the need for local calibration of atmospheric parameters and performs well over global atmospheric conditions (Jiménez-Muñoz et al., 2014).

Here, we present the LakeTEMP dataset, consisting of two separate subsets termed "Primary" and "Aggregated" (Fig. 1). The Primary dataset comprises quality controlled LSWT data at the centers of the 1,427,688 lakes contained in the HydroLAKES database. Landsat 8 has a revisit time of ~16 days, so roughly bi-monthly observations were available for consideration between 2013 and 2021. The Aggregated dataset is intended as a ready-to-analyze product and contains summary statistics, interpolated from the Primary dataset. This includes the average yearly and average monthly mean, minimum, and maximum LSWTs (± 95% confidence intervals), as well as estimations of ice phenology (average yearly duration of ice cover and the approximate average ice on and ice off dates, ± 95% confidence intervals). We used thorough quality control methods and provided quality flags with both datasets, validated the Primary data with in-situ data, and compared the Aggregated data to other in-situ and satellite-derived LSWT and ice
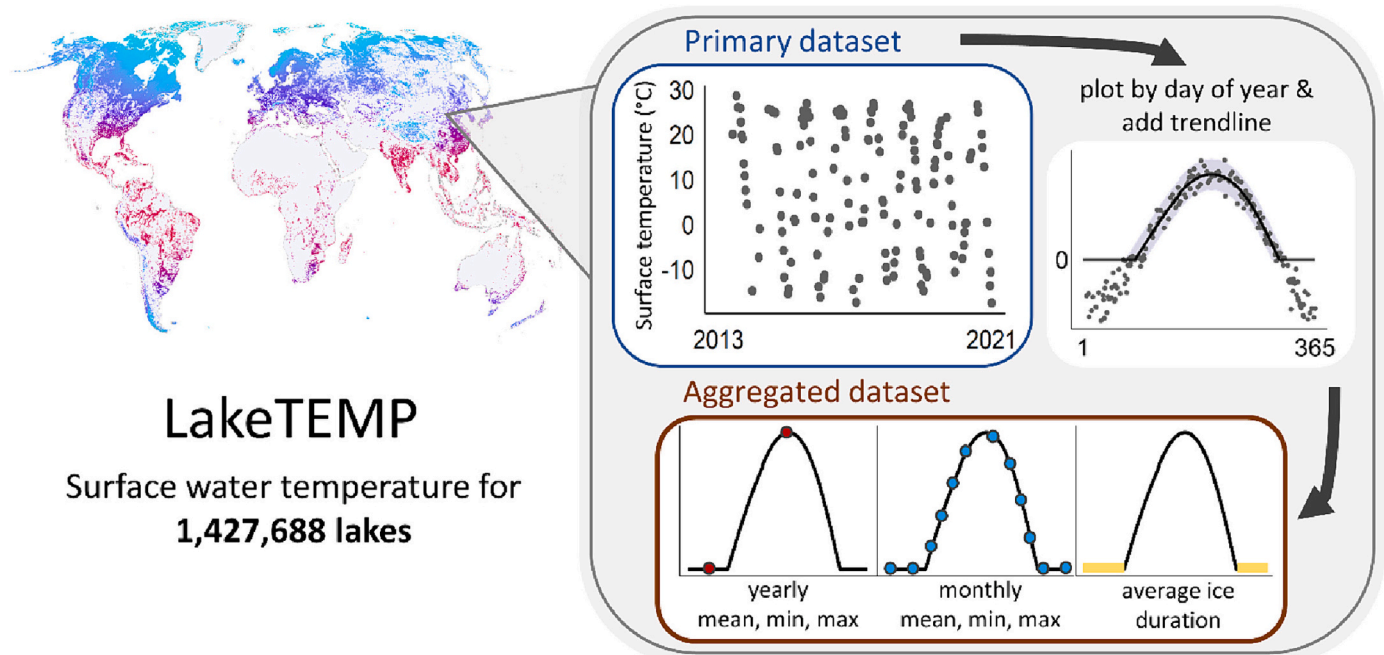
Fig. 1. Overview of the LakeTEMP dataset and its two subsets. The Primary dataset comprises weekly to monthly discrete LSWT data for the period 2013–2021. The Aggregated dataset comprises average yearly and average monthly mean, minimum, and maximum LSWTs (± 95% confidence intervals), and ice phenology predictions (average yearly duration of ice cover and the approximate average ice on and ice off dates, ± 95% confidence intervals), derived from the Primary data using seasonal trendlines.

phenology datasets. Finally, we present an overview of LSWT conditions between 2013 and 2021 and highlight large-scale spatial variations in LSWT across lakes globally. All data are available in CSV files to lower the barrier for data users not versed in handling massive raster-based spatial datasets (Ramachandran et al., 2021) and the data employ the unique lake identifiers from HydroLAKES, so that they can be easily combined with other lake datasets that use the same hydrography (e.g., LakeATLAS (Lehner et al., 2022)).

2. Methods

2.1. Primary dataset: lake surface water temperature observations

2.1.1. Data processing

Lake surface water temperature (LSWT) is the temperature of the upper layer of the water surface, which in the case of satellite observations corresponds to the thin layer (<0.1 mm thick) from which thermal radiation is emitted. The Primary dataset was derived from thermal wavelength bands 10 (10.60–11.19 μm) and 11 (11.50–12.51 μm) of the Landsat 8 top-of-atmosphere reflectance collection 1 (United States Geological Survey, 2021), calculated for a narrow (50 m) buffer surrounding the center point location of each lake. This location and buffer selection was an important step in minimizing the risk of land surface inclusions in observations from small lakes, while ensuring that more than one pixel per lake could be used for calculations. Following the approach by Carrea et al. (2015), we defined the center point of a lake to be the single location inside the lake that is the furthest away from any lake shore or island, as detailed in Appendix A.1. Shoreline polygons were provided by the HydroLAKES database (Messager et al., 2016), which includes both natural (1,420,891) and artificial (6797) lakes of at least 0.1 km² in surface area, which are both referred to as 'lakes' throughout this work.

Although preceding Landsat missions (Landsat 4, 5, and 7) provide TIR measurements since 1982, we chose not to include those data to avoid inconsistencies in the quality as well as frequency of the data record. Most importantly, the sensors on board Landsat 4, 5, and 7 collected TIR measurements in one channel, requiring a single-channel (SC) algorithm to calculate LSWT. A SC algorithm needs local calibration of atmospheric conditions and is therefore not suitable for global applications. Furthermore, Landsat 4 suffered sensor failures within a year of its launch, Landsat 5 data contain a considerable data gap between the years 2000 and 2003, and Landsat 7 is affected by data gaps since 2003. Despite these deficiencies, we investigated whether the addition of Landsat 7 observations to the Landsat 8 record would strengthen the dataset through an analysis with in-situ LSWT data (see Appendix A.2 for further detail), but we found that the overall data quality decreased.

The Google Earth Engine platform was used to download the TIR imagery and to perform initial processing steps. First, every pixel that was fully or partially covered by clouds, cloud shadows, or cirrus clouds, was masked, using the medium and high cloud confidence levels (i.e., 33–100%) from the Quality Assessment bands provided with the Landsat 8 collection. Second, each image was matched with a 2.5-degree and 6-h resolution water vapor raster dataset (NCEP/NCAR Reanalysis Water Vapor product; Kalnay et al., 1996) by taking the two water vapor rasters closest in time and interpolating the pixel values. Then, LSWT was calculated and corrected for water vapor using the SW algorithm of Jiménez-Muñoz et al. (2014):

$$T = T_i + c_1\left(T_i - T_j\right) + c_2\left(T_i - T_j\right)^2 + c_0 + (c_3 + c_4 w)(1 - \varepsilon) + (c_5 + c_6 w)\Delta\varepsilon$$

(1)

where T is the surface temperature in Kelvin, T_{10} and T_{11} are the at-sensor brightness temperatures at bands 10 and 11, w is the total atmospheric water vapor content (in g cm^{-2}), ε is the mean of emissivity values 0.998 (ε_{10}) and 0.992 (ε_{11}), as tested for both waterbody and

wetland surface classes by Du et al. (2015), $\Delta\varepsilon$ is the emissivity difference ($\varepsilon_{10} - \varepsilon_{11}$), and c_0 to c_6 are constants, defined by Jiménez-Muñoz et al. (2014) as −0.268, 1.378, 0.183, 54.30, −2.238, −129.20, and 16.40, respectively. Even though some studies use the SC algorithm by Jiménez-Muñoz et al. (2009) to calculate surface temperature from Landsat 8 observations (e.g., Ermida et al., 2020), we found that, based on an analysis with in-situ data, the SW performed better (see Appendix A.2 for further detail).

Finally, a weighted average LSWT was calculated from all pixels within a 50 m × 50 m square buffer around each lake center point, where pixel weights were determined by the fraction of the pixel covered by the buffer. The number of pixels (including fractions) contained in each buffer zone ranged from ~2 near the equator to ~6 in the subarctic and ~14 near the northern extent of this dataset (81°). Throughout this work, the word 'observation' refers to pixel averaged LSWT data. The temporal resolution of the dataset is generally around 16 days, but it can range from multiple observations a week to only a few observations per year depending on latitude (increased number of observations due to shorter Landsat revisit intervals at higher latitudes), cloud conditions (cloud contaminated observations were removed) and potential lateral overlap between orbital paths (increasing the number of observations).

2.1.2. Data filtering and quality control

Observations were flagged or removed based on three criteria: imagery overlap, lake intermittency, and statistical outliers. Lateral overlap provided additional observations taken several hours (at the poles) to days (at lower latitudes) apart, but forward overlap provided observations taken only seconds to minutes apart, which introduced a bias when calculating statistics for the Aggregated dataset. Therefore, observations taken within the same hour were consolidated (averaged) or removed if their values differed by >0.2 °C (3% of overlapping data). This procedure reduced the number of observations from the original dataset by 14%. By transferring monthly water occurrence information from the Global Surface Water dataset (Pekel et al., 2016) at the lake center locations, all observations were flagged with values 1 to 4 for 'water', 'land', 'unknown', and 'no information', respectively, where frozen water surfaces fall under the 'unknown' class and 'land' surfaces represent dry lake beds. More details on these extraction procedures are given in Appendix A.3. Furthermore, we used a lake-specific and seasonally varying statistical threshold to flag observations as outliers, which is an approach recommended for LSWT timeseries by Woolway et al. (2021). Specifically, we calculated a *Z-score* for each observation from a seasonal trendline and a rolling standard deviation:

$$Z_i = \left(y_i - \check{y}_i\right)\Big/\sigma_s$$

(2)

where y_i is the LSWT of observation i, $\check{y}_i$ is the LSWT of observation i predicted from the trendline, and σ_s is the residual standard deviation calculated from the number of observations (n_s) in a 90-day window around observation i:

$$\sigma_s = \sqrt{\frac{\sum_{i=1}^{n_s}\left(y_i - \check{y}_i\right)^2}{n_s - 1}}$$

(3)

The 90-day window was used to ensure a maximum sample size for the calculation of σ_s, while only capturing observations sharing similar meteorological conditions. However, if n_s was <30 (i.e., the minimum sample size required for a normal distribution), σ_s was calculated from all observations in the timeseries. We plotted and visually checked *Z-score* thresholds ranging from 2.5 to 4, values suggested by Hair et al. (2010), on ~600 randomized but geographically evenly distributed timeseries. We chose the more cautious threshold of $Z = \pm4$ to avoid the unwarranted flagging of observations recorded during extreme weather conditions, which according to Woolway et al. (2021) can occur well

above a 90th percentile threshold. Seasonal trendlines were generated with a Generalized Additive Model (GAM), a technique that uses smooth functions to predict non-linear regression trends (Wood, 2017). If the number of LSWT observations in a timeseries was <12 (0.8% of all timeseries), a trendline could not be applied and outliers were therefore not detected. More details on the GAM calculations are given in Appendix A.4. Finally, observations <0 °C were not removed from the dataset because they were used for the estimation of ice phenology (section 2.2.2). However, these values should not be interpreted as ice surface temperatures, which require a different, locally calibrated algorithm for their calculation (Liu et al., 2018).

2.1.3. Validation with in-situ data

The LSWT observations were validated against in-situ LSWT observations from 48 lakes across 5 continents, of which 13 large lakes provided data for multiple sites thus representing 63 sites in total (Fig. 2a).
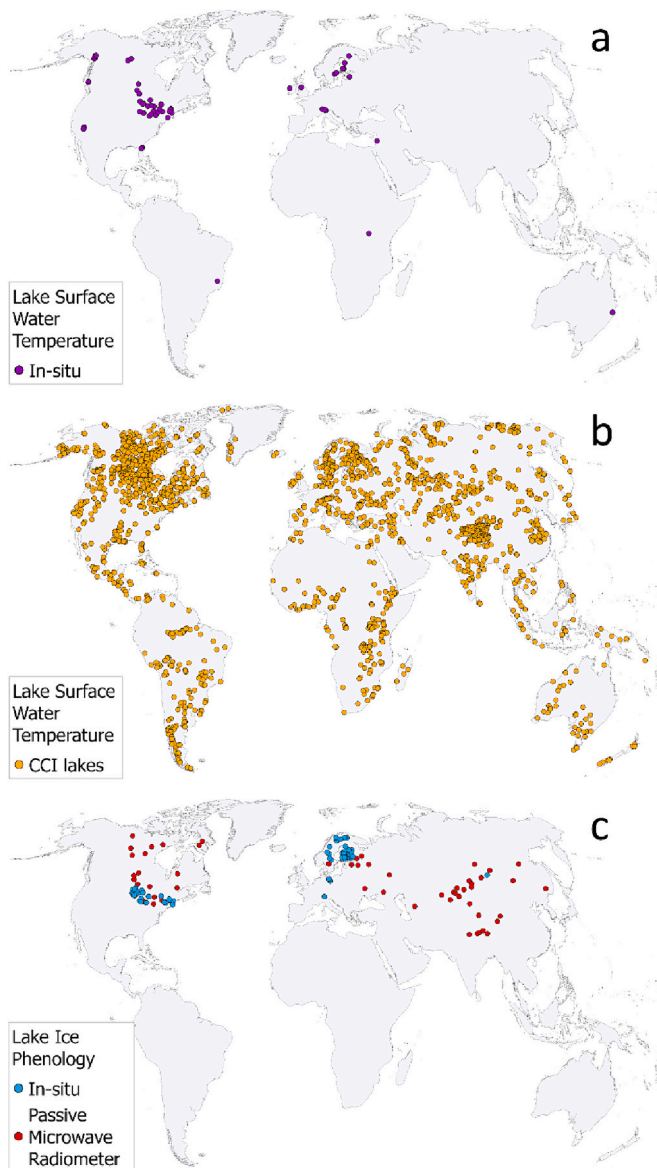
Fig. 2. Locations of lakes used for a) validation of LSWT observations with in-situ data, b) comparison of mean monthly LSWT with data from the European Space Agency Climate Change Initiative (CCI; Carrea et al., 2022, 2023), and c) validation of ice phenology estimations with in-situ (Benson et al., 2020) and passive microwave radiometer (Cai et al., 2021, 2022) ice phenology observations.

In-situ data were acquired from individual as well as public sources, specified and cited in the Acknowledgements and Table A.1, after intensive searches for high-quality and accessible data. Continuous data (measured from a permanent buoy) were required as manual measurements rarely match local satellite overpass times. At most sites, the buoy was installed within the first meter below the water surface and during the open water season only, but at a few high-latitude sites they were installed deeper (up to 2.5 m) to measure under-ice temperature in winter. These winter measurements were removed based on ice phenology records, either provided by the data sources, or else estimated from visual inspections of Sentinel-2 satellite imagery. In addition, we performed automated checks and manual inspections on all records to flag and remove unrealistic data (e.g., negative readings or large outliers). Landsat 8 observations were extracted from the locations of the field buoys and quality controlled as described in section 2.1.2, whereas outliers and observations <0 °C were removed. The observations were then matched with the in-situ data by date and hour ($n = 52$) or only date ($n = 12$), depending on the format of the in-situ data (Table A.1). In addition to the validation of the LSWT observations, the in-situ data were used to validate the flags indicating dry surfaces (section 2.1.2), as it is highly unlikely that the in-situ data were recorded during dry conditions. For this analysis, data from the Global Surface Water dataset (Pekel et al., 2016) were extracted for the in-situ locations (Appendix A.3) and matched with the in-situ temperature observations by month and year.

2.2. Aggregated dataset: annual and monthly average lake surface water temperature and ice cover

2.2.1. Surface water temperature

Annual and monthly LSWTs were calculated from a seasonal trendline fitted through each LSWT timeseries in the Primary data, by taking the mean, maximum, and minimum of the 365 or 28 to 31 daily trendline values, respectively (Fig. 1). The trendline approach was chosen because data gaps often concentrate around seasons experiencing cloud-cover and calculating statistics from LSWT observations directly would introduce bias. Trendlines were generated with a GAM, which has the ability to predict the continuation of a trend throughout timeseries gaps and to track seasonal LSWT patterns that are not strictly harmonic (more details on the GAM calculations are given in Appendix A.4). Outliers or observations that were flagged as dry surfaces (section 2.1.2) were not used in the GAM calculation. Furthermore, if the number of filtered LSWT observations in a timeseries was <12, a trendline could not be applied and only the yearly mean, maximum, and minimum LSWTs were calculated from the observations directly. Trendlines can get skewed when anomalously high or low LSWT observations – that divert from the mean but are not necessarily invalid (i.e., recorded during extreme weather conditions) – are available for periods that are otherwise data sparse. To correct for this, trendlines were plotted twice: first to flag extreme LSWT values using a *Z-score* threshold (Eqs. 2 and 3), and second using the resulting filtered observation timeseries. As it was especially important to flag extreme values during data sparse periods and it is recommended to use lower *Z-score* values for smaller sample sizes (Hair et al., 2010) we chose a threshold of $Z = \pm 2$, which was visually checked on ~600 randomized but geographically evenly distributed timeseries plots. Negative LSWT observations were retained for trendline plotting as these were assumed to occur when lake ice was present, even though exact values cannot be interpreted as ice surface temperatures. Trendline values <0 °C were then set to 0 °C, which was the assumed temperature of the water layer directly under the ice.

2.2.1.1. Uncertainty calculations and quality flags.

For regression models like GAMs, confidence intervals (CIs) can be calculated to account for uncertainty in the estimation of the mean (i.e., the uncertainty of the LSWT trendline fit), or to predict measurement ranges (i.e., the

likelihood that a LSWT observation falls within certain bounds) (von Storch and Zwiers, 1999). Both cases were calculated for every observation i of a lake's timeseries at a 95% confidence level:

$$CImean_i = \check{y}_i \pm t_{0.975} * \sigma_s * \sqrt{\frac{1}{n_s} + \frac{(x_i - \bar{x}_s)^2}{\sum_{i=1}^{n}(x_i - \bar{x}_s)^2}} \qquad (4)$$

$$CIpred_i = \check{y}_i \pm t_{0.975} * \sigma_s * \sqrt{1 + \frac{1}{n_s} + \frac{(x_i - \bar{x}_i)^2}{\sum_{i=1}^{n}(x_i - \bar{x}_i)^2}} \qquad (5)$$

where *CImean* is the upper or lower bound of the trendline prediction $\check{y}$, *CIpred* is the upper or lower bound of the predicted measurement range, $t_{0.975}$ is the 97.5% quantile of the t-distribution, σ_s is the 90-day rolling standard deviation (Eq. 3), n_s is the number of observations in a 90-day window around observation i, x is the Julian day, and $\bar{x}_s$ is the mean Julian day of all observations in a 90-day window around observation i. The 90-day window was used to ensure a maximum sample size, while only capturing observations sharing similar meteorological conditions. However, if $n_s < 30$, all timeseries observations were used to calculate n_s, σ_s, and $\bar{x}_s$. These calculations did not include LSWTs < 0 °C, observations that were flagged as dry surfaces, or outliers (section 2.1.2), but did include observations that were flagged as outliers during trendline fitting. Both CIs were linearly interpolated between Julian days to obtain 365 daily confidence bounds, which were averaged to obtain the uncertainties around the yearly and monthly means and the monthly predictions of measurement ranges. Finally, as with the trendlines, confidence bound values < 0 °C were set to 0 °C.

Three variables with data quality information were provided: the number of observations used for calculations, the method used (i.e., from trendline or direct), and the likelihood that a lake experienced intermittency. Although observations taken during dry periods were removed from the timeseries prior to calculating statistics, the resulting data gaps can still have influenced the calculations. For example, the interpolation of a trendline through an intermittent lake's dry season can skew the resulting yearly mean, maximum, or minimum LSWT towards these predictions. The likelihood and the level of lake intermittency was flagged using six categories. Descriptions and interpretations of the method and intermittency categories, as well as the potential consequences for the quality of the data, are provided in Table 1.

2.2.1.2. Comparisons with in-situ and other satellite data. The adequacy of the trendline to predict mean LSWT was tested by comparing monthly mean LSWTs to the monthly mean LSWTs calculated from in-situ data (Table A.1) and a satellite derived data product. Monthly mean LSWTs were calculated from the in-situ data directly, for months with >27 or >670 data points for daily and hourly timeseries, respectively (providing 405 monthly data points from 54 sites). The satellite derived LSWT product was released in 2022 by the European Space Agency Climate Change Initiative (Carrea et al., 2022, 2023; hereon referred to as 'CCI data'). Precursors to the CCI data have been widely used for studies investigating the effects of climate change on global lakes (e.g., Woolway et al., 2022; Woolway and Merchant, 2019), and we chose this dataset due to its high-temporal resolution and global coverage. The current version of the CCI data provides daily average LSWT observations (1995 – 2021) from ATSR2 (ERS-2), AATSR (Envisat), MODIS (Terra), AVHRR (MetOpA and MetOpB), and SLSTR (Sentinel3A and Sentinel3B) sensors in a $1/120°$ grid format (~1 km resolution at the equator) for 2024 lakes across the world. All data are accompanied by quality level flags that were established from a reflectance-based water detection and distance from shore. We extracted daily LSWT observations from the CCI data between 2013 and 2021 from the pixel overlapping the locations that were used for extracting Landsat 8 data. Only observations with the highest quality levels (4 and 5) were kept and

Table 1

Quality level flagging scheme of the Aggregated dataset, with flag definitions based on the underpinning Primary dataset, interpretations of the lake types associated to each flag, consequences for the data, and the % of lakes affected (out of 1,427,688). The definitions of the 'intermittency' flags are given by the % of timeseries observations that were acquired from 'water', 'land' (representing dry lake beds), 'unknown' (including snow or ice surfaces), or 'no information' surfaces, as derived from Pekel et al. (2016) (see Appendix A.3 for more details). Interpretations are descriptions of the likely condition of a lake during data acquisition, however other interpretations are possible.

Flag	Definition	Interpretation	Consequences	% of lakes
Calculation method				
0	From trendline; ≥ 12 observations	All regions/lake types	Full set of statistics calculated from trendline	98.8
1	Direct; <12 observations	Lake in high cloud-cover area or intermittent/ ephemeral lake	Only yearly mean, min, max calculated directly	0.8
NA	No observations	No observations due to permanent cloud cover or intermittency flag 4	No statistics calculated	0.4
Intermittency				
0	$\leq 20\%$ 'land' over 'water' observations	Perennial lake, or dry for periods that are not long enough to affect calculations considerably	'Land' observations removed before calculation	87.2
1	$>20\%$ and $\leq 80\%$ 'land' over 'water' observations	Intermittent lake	'Land' observations removed before calculation	6.2
2	$>80\%$ 'land' over 'water' observations	Ephemeral lake or intermittent lake with long dry season	'Land' observations removed before calculation	2.7
3	100% 'land' + 'unknown' observations	Permanently dry lake with seasonal snow or ice cover	Statistics calculated from 'unknown' readings only	3.4
4	100% 'land' observations	Permanently dry lake; or wetland with dense vegetation	No statistics calculated	0.3
5	100% 'no information'	Lake near north pole; or lake in area with high cloud cover; or other unknown issues	Statistics calculated from all observations	0.2

matched to their corresponding Landsat 8 observations by lake and day. Monthly mean LSWTs were then calculated from the CCI data directly, but only if there were >90 observations (per month) available over the full record period. This selection procedure generated a dataset of 4095 data points for a comparative analysis on 1231 lakes (Fig. 2b).

2.2.2. Ice cover

The average yearly duration of lake ice cover was estimated by the count of all days on which the LSWT trendline (section 2.2.1) was equal to 0 °C and the average ice on and ice off dates (Julian day) were approximated as the start and end occurrences, respectively, of 0 °C. If no trendline was plotted due to a lack of observations (i.e., <12), no ice phenology data were calculated. When multiple freezing periods were modelled per year (0.05% of lakes), the first ice on and the last ice off days were recorded whereas intermediate start or end occurrences were not specified in the dataset. However, the smaller number of ice cover

duration days compared to the period between ice on and ice off dates can be used to identify this phenomenon.

2.2.2.1. Uncertainty calculations and quality flags. Upper and lower estimates of average yearly ice cover duration, ice on, and ice off dates, were calculated from the 95% measurement prediction ranges (*CIpred*; Eq. 5) around the LSWT trendlines. The ice phenology calculations described above were repeated on the daily upper and lower bounds of *CIpred,* whereas the lower ice phenology estimates were derived from the upper bounds and the upper ice phenology estimates were derived from the lower bounds. No quality flags specific to the ice phenology estimations were added, however the number of observations, calculation method, and lake intermittency flags (section 2.2.1.1 and Table 1) apply to the overall quality of the Aggregated dataset, including the ice cover estimations.

2.2.2.2. Comparisons with in-situ and other satellite data. The estimations of average yearly ice cover duration were compared to the in-situ ice phenology records from the Global Lake and River Ice Phenology Database (Benson et al., 2020), and the records of 56 lakes across the northern hemisphere that were derived from Passive Microwave Radiometer (PMR) imagery by Cai et al. (2021, 2022) (Fig. 2c). The in-situ database consists of freeze up and break up dates for 409 lakes and rivers in North America and Eurasia, as observed visually on site. From these lakes, 318 did not have sufficient records (at least 2 years of observations) after the year 2013, four were too small to occur in the HydroLAKES dataset (<0.1 km^2), and three were a subbasin of a larger, overarching lake in HydroLAKES. For the remaining 84 lakes, the available records ($n = 189$) were averaged to obtain yearly ice cover durations. The PMR database provides ice phenology as the duration between start of freeze up and the first day of complete break up, and as the duration between whole lake freeze up and the start of break up, which were both assessed. No records were available after the year 2013 for the Large Aral Sea, and no Landsat 8 observations or ice cover predictions were available for the Caspian Sea, but for the 54 other lakes, the observations taken between 2013 and 2019 ($n = 316$) were averaged to calculate yearly ice cover durations.

3. Results

3.1. Primary dataset: lake surface water temperature observations

Considering Landsat's repeat cycle of 16 days, around (but no more than) 180 observations per timeseries (2013 – 2021) would be expected. However, excluding the observations masked by clouds, the observations acquired from dry surfaces, and outliers, and including observations from overlapping imageries (taken >1 h apart), the number of timeseries observations ranged from 0 to 1587, with a median of exactly 100 (Fig. 3). Overall, the number of observations increased with latitude due to the increase in lateral imagery overlap. In addition, smaller-scale variations were driven by cloud cover (e.g., few observations below the intertropical convergence zone and rainward sides of major mountain ranges) and degree of intermittency (Table 1). No imagery was available for the center point location of the Caspian Sea, and no valid observations were available for 66 lakes with consistent cloud cover and for 4309 lakes that were consistently dry at their center points.

3.1.1. Validation with in-situ data

To assess data quality, the root mean square error (RMSE) was used to evaluate data precision, and the median of differences (MOD; calculated from in-situ LSWT minus Landsat 8 LSWT values) was used for accuracy, in addition to the overall goodness-of-fit (R^2). Across the full set of LSWT validation data (63 sites with a total of 2074 observations matching Landsat 8 overpass times; Fig. 2a), the R^2 was 0.93, the RMSE was 1.71 °C and the MOD was 0.42 °C, with the positive MOD value indicating an overall slight bias towards underestimating LSWT with Landsat 8. A trendline plotted through the distribution of LSWT differences (Fig. 4) indicates that this bias decreases from ~1.8 °C at near-zero temperatures to ~0.4 °C at temperatures above 28 °C. Table A.2 lists all validation results by lake.

Seven percent of the Landsat 8 vs. in-situ observation pairs in the validation dataset were >3 °C different from each other, and in most cases (88%) Landsat 8 observations were cooler than the in-situ data. These cooler observations at in-situ locations were often acquired from imageries that were affected by cloud cover (Fig. 5), more specifically from locations around the cloud edges, which were not covered by the cloud mask provided by Landsat 8. This could presumably point to the rapid cooling of the skin water surface located below a cloud shadow (and thus a valid observation), or to a sensor reading anomaly likely caused by localized high atmospheric water vapor. The Landsat 8
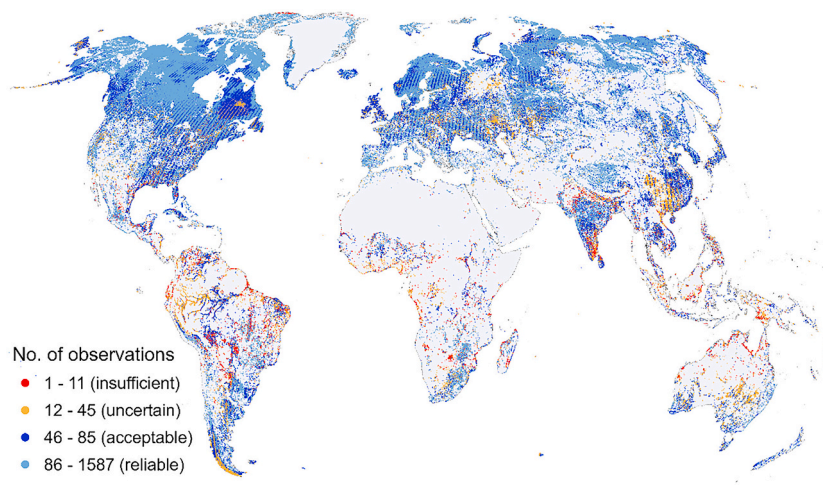
Fig. 3. Number of surface water temperature observations taken at the center of each lake in the Primary dataset. Classes indicate how the Aggregated data, calculated from the Primary data, can be considered reliable, acceptable, uncertain, or insufficient, based on the number of observations per lake timeseries (see section 4.1 for more detail). These numbers exclude observations masked by clouds, taken from dry surfaces, and outliers, and include observations from overlapping imageries (taken >1 h apart) and observations <0 °C.
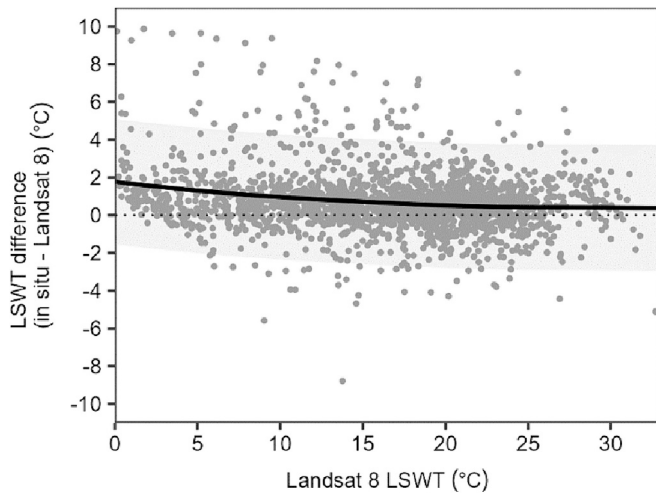
Fig. 4. Differences in LSWTs between Landsat 8 and in-situ measurements (*n* = 2074). Landsat 8 LSWTs were acquired at in-situ buoy locations. The trendline (solid line) with 95% measurement prediction intervals (shaded area) was generated with a Generalized Additive Model (GAM) and shows the central bias across the range of Landsat observations acquired for the in-situ validation (0–32.7 °C). The dotted line emphasizes zero-difference for reference.
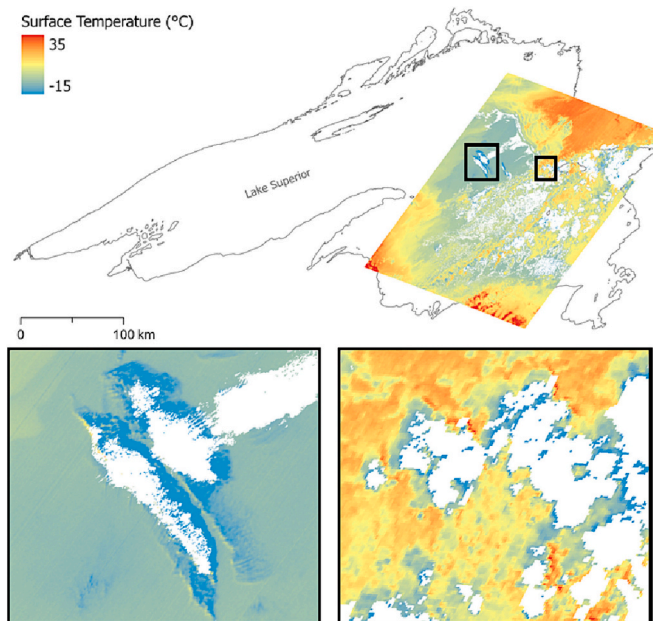
Fig. 5. Surface temperature imagery (2014-07-21 04:33, LC08_023027) of Lake Superior (Canada/USA) from Landsat 8. Transparent (white) areas are the pixels that have been masked out due to clouds. The insets show two examples of the 'cloud edge' problem: around the edges of the masked areas, temperatures are cooler than the surrounding surface temperature. This could either point to a sensor anomaly, or to rapid skin water surface cooling when a cloud shadow passes.

observations that were warmer than the in-situ data were generally taken during days in early summer after ice break-up and when air temperatures were especially hot compared to the preceding and succeeding days. In addition, about half of these measurements were from three Arctic lakes that had buoys installed at 2.5 m depth. Therefore, we presume that warmer Landsat 8 observations do not point to sensor anomalies, but rather display how daytime warming can develop steep temperature gradients between the warm upper water surface and cooler in-situ sensor depths (Wilson et al., 2013).

Matching the in-situ observations with the 'water', 'land', or 'unknown' classes derived from the Global Surface Water dataset (Pekel et al., 2016), and assuming that all in-situ data must have been collected during 'water' conditions, revealed that 68.0% of all Landsat 8 observations of the validation dataset were correctly classified as 'water', 31.7% were classified as 'unknown', and 0.3% were wrongfully classified as 'land'.

3.2. Aggregated dataset: annual and monthly average lake surface water temperature and ice cover

3.2.1. Surface water temperature

The global average surface water temperature was found to be 6.3 °C (assuming 0 °C during times of presumed ice cover) and 12.4 °C when only considering periods of open water (i.e., when trendline LSWT >0 °C). This was calculated from the 365 daily trendline values derived for each lake, except the 179,524 lakes (12.6% of dataset) that were flagged for potential intermittency (levels 1 to 4, Table 1) and the 11,437 lakes with <12 LSWT observations (0.8% of dataset). Ninety percent of all lakes recorded average temperatures below 10.0 °C (assuming 0 °C under-ice temperatures) and 15.5 °C (open water only) (Fig. A.2). These low average temperatures are driven by the high concentration of lakes at mid to high latitudes in the northern hemisphere (i.e., 92% of lakes are above 45°N). The global average surface water temperature that is more representative of all climatic regions, calculated by first averaging all lake temperatures (including under-ice estimations) within one-degree latitude bins (56°S – 84°N), was 15.9 °C, with the highest average LSWTs of around 30 °C recorded between 20°S and 20°N (Fig. 6). Mean LSWT also showed a correlation with elevation, as temperatures were below the latitudinal average in the mountain ranges of the Rockies, Pacific Coast, Andes, Tibetan Plateau, Turkistan, Altai, Alps, and Scandes. Global monthly average surface water temperatures (including under-ice estimations) ranged from 1.3 °C in December, January, and February, to 17.6 °C in July (Table 2). Yearly mean LSWT confidence intervals (95%) were generally (i.e., for 95% of lakes) within ±1.2 °C, with monthly confidence intervals ranging between ±1.6 °C in July and ±2.9 °C in January. The yearly range in LSWT (i.e., maximum minus minimum daily average LSWT) was highest for lakes in the mid-latitudes, with ranges of up to 46 °C recorded in small and shallow lakes in the Ryn desert of western Kazakhstan. Other extremely high, but rare, temperature ranges (between ~35 and ~46 °C) and mean temperatures (between ~33 and ~36 °C) were generally recorded in small and shallow artificial lakes, used for power generation, mining, salt extraction, and aquaculture.

3.2.1.1. Comparisons with in-situ and other satellite data.
We compared the Landsat 8 monthly mean LSWTs derived from each lake's trendline with the monthly mean LSWTs derived from the in-situ measurements (54 sites, 405 monthly data points) and the CCI data (1231 sites, 4095 monthly data points) directly. This revealed an R^2 of 0.97, an RMSE of 1.23 °C and a MOD of 0.80 °C (in-situ minus Landsat 8) and an R^2 of 0.99, an RMSE of 0.81 °C and a MOD of 0.42 °C (CCI minus Landsat 8), respectively, indicating a better agreement with the CCI data and an overall slight bias towards cooler Landsat 8 observations. Trendlines plotted through the distributions of mean LSWT differences (Fig. 7) indicate that this bias is higher (differences with a central tendency between 1 and 3 °C) in the near-freezing range. Accordingly, lakes with mean monthly LSWTs >2 °C cooler than the CCI data (4% of CCI lakes) were mostly located in cold, northern high-latitude environments. We also compared the direct LSWT observations of the Landsat 8 and CCI datasets to test for instrument bias and found an R^2 of 0.97, an RMSE of 1.17 °C and a MOD of 0.33 °C. This, together with the in-situ validation results described in section 3.1.1 (R^2 of 0.94, RMSE of 1.71 °C and MOD of 0.42 °C), indicates that the trendline calculations improved the R^2 by ~0.02, added a minor additional bias (MOD) of 0.38 and 0.09 °C, and
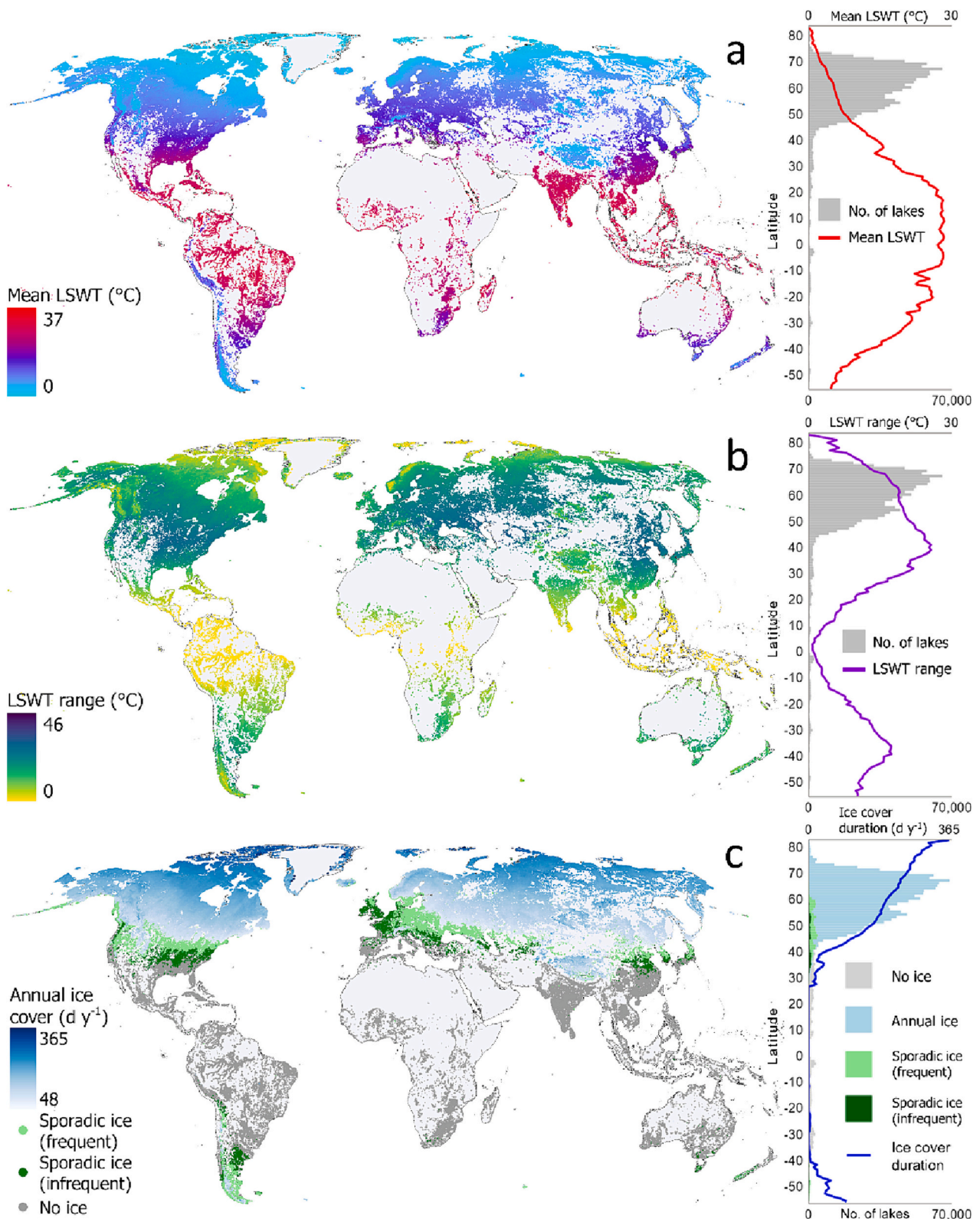
Fig. 6. The yearly mean LSWT (a), the yearly range in LSWT (b), and the yearly duration of ice cover (c) for the center points of ~1.4 million lakes, based on Julian day averages over 2013–2021 (left) and averaged by one-degree latitude bins (right). Lakes with <12 LSWT observations are not shown in panels a, b, and c, and lakes that were flagged for potential intermittency (levels 1 to 4, Table 1) are not shown in panels a and b. Ice cover classes are based on statistical likelihoods: 'annual ice cover' is assumed when the predicted ice cover duration, including lower and upper estimates, was >0 days; 'sporadic (frequent) ice cover' when predicted ice cover was >0 days, but with a lower estimate of 0 days; 'sporadic (infrequent) ice cover' when the predicted ice cover was 0 days, but with a higher estimate of >0 days; and 'no ice cover' when the predicted ice cover, including lower and upper estimates, was 0 days.

Table 2

Summary statistics of lake surface water temperature (LSWT) and ice cover, by month and by ice class (explained in section 3.2.2). Mean and median average (2013–2021) LSWTs are calculated including / excluding under-ice estimations of 0 °C, from lakes that had ≥12 LSWT observations and were not flagged for potential intermittency (86.6% of dataset). Average ice cover statistics were calculated from all lakes with ≥12 observations. A lake was assumed to be ice covered if for the entire duration of a month LSWT measured 0 °C.

	Average LSWT		Average ice cover		
	Mean (°C)	Median (°C)	% of lakes	Lake area (km^2)	Lake area (%)*
Month					
Jan	1.3 / 17.1	0.0 / 19.3	89.6	1,680,274	65.9
Feb	1.3 / 15.3	0.0 / 14.3	88.2	1,650,787	64.7
Mar	1.6 / 12.7	0.0 / 9.7	83.3	1,596,238	62.6
Apr	2.3 / 6.1	0.0 / 1.8	56.6	948,644	37.2
May	5.8 / 7.2	3.1 / 5.1	16.0	336,572	13.2
June	12.5 / 12.6	12.7 / 12.8	0.8	61,942	2.4
Jul	17.6 / 17.7	18.3 / 18.3	0.9	48,281	1.9
Aug	16.8 / 16.9	16.9 / 16.9	0.8	45,831	1.8
Sep	9.8 / 9.9	8.7 / 8.8	0.9	47,799	1.9
Oct	3.3 / 5.3	0.4 / 2.1	32.6	314,407	12.3
Nov	1.7 / 9.0	0.0 / 3.7	77.1	1,061,791	41.6
Dec	1.3 / 14.1	0.0 / 12.2	87.4	1,503,287	59.0
Ice class					
Annual ice	5.1 / 11.7	4.9 / 12.0	86.1	1,446,187	57.0
Sporadic ice	11.7 / 13.8	11.9 / 14.0	6.0	492,550	19.5
No ice	24.4 / 24.4	25.8 / 25.8	7.9	595,361	23.5

* Total lake area (2,534,279 km^2) calculated without the areas of lakes with <12 observations, which includes the Caspian Sea (377,002 km^2).

Fig. 7. Mean monthly lake surface water temperatures (LSWTs) from Landsat 8, calculated from each lake's trendline, compared to mean monthly LSWTs calculated directly from a) in-situ data ($n = 405$), and b) data from the European Space Agency Climate Change Initiative ($n = 4095$) ('CCI'; Carrea et al., 2022; Carrea et al., 2023). Trendlines (solid lines) with 95% measurement prediction intervals (shaded areas) were generated with a Generalized Additive Model (GAM) and show the central bias across the range of Landsat mean monthly LSWTs (0–32.7 °C). The dotted line emphasizes zero-difference for reference.

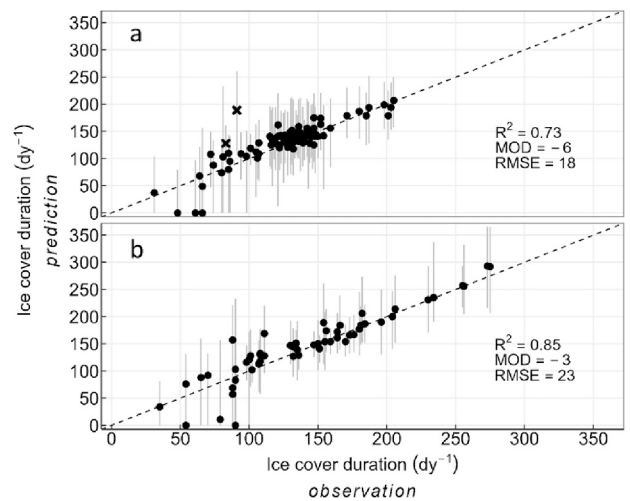improved precision (RMSE) by 0.48 and 0.36 °C, regarding the in-situ and CCI data, respectively.

3.2.2. Ice cover

Of all lakes with 12 or more LSWT observations, 7.9% never froze between 2013 and 2021 at their center point (Fig. 6). This was determined by identifying the lakes with a predicted yearly ice cover of 0 days, including upper and lower estimates of ice cover duration. These lakes were located between 52°S (southern Chile) and 57°N (Scotland, Loch Ness). Another 6.0% of lakes were predicted to freeze sporadically between years. Of these lakes, 4.1% had a higher likelihood to freeze, and thus freeze more frequently (predicted ice cover of >0 days, but with a lower estimate of 0 days), than the other 1.9% (predicted ice cover of 0 days, but with a higher estimate of >0 days). This leaves 86.1% of lakes that, based on our statistical analysis, froze annually. Within the annual ice cover class, average ice cover durations ranged from 48 days to year-round, with a mean duration of 213 days. This means that if an average duration of ice cover <48 days was predicted, the lake is unlikely to experience recurring, annual freezing periods. Additional ice cover statistics aggregated by month and by freezing class (i.e., annual, sporadic, and no ice cover), including estimated global areas of frozen lake surfaces, are given in Table 2.

3.2.2.1. Comparisons with in-situ and other satellite data.
We found a clear relationship between the average ice phenology from in-situ observations of 84 lakes, and the average ice phenology predicted from Landsat 8 ($R^2 = 0.73$; Fig. 8a). In terms of absolute differences, the average yearly durations of ice cover predicted with Landsat 8 observations were about six days longer than in-situ observations (MOD = −6

Fig. 8. Comparison of the average yearly ice cover durations (2013–2021, in days per year) as predicted with Landsat 8 observations and a) as observed in-situ for 84 lakes in North America and Eurasia (Benson et al., 2020), and b) as observed from Passive Microwave Radiometer measurements for 54 lakes in North America and Eurasia (Cai et al., 2021, 2022). The dotted line indicates a 1:1 relationship, the MOD is the median of differences in days (observation minus Landsat 8 prediction) and the RMSE is the root mean square error in days. Error bars are the upper and lower estimates of ice cover duration based on 95% measurement prediction ranges around the LSWT trendlines. A point is marked by a cross if an observation does not fall within these estimates.

days), the RMSE was 18 days and differences in durations (in-situ minus Landsat 8) ranged between −98 and +66 days. However, including the upper and lower estimation bounds of ice cover duration, all predictions but two matched the in-situ observations. One non-match can be explained by the short in-situ record (3 years), of which one year had an anomalously short ice season. The other non-match, Lake Baikal in Russia, can be explained by its large water volume and depth which causes high thermal inertia. Ice cover predictions were better for lakes with long ice seasons (in-situ duration >100 days; $R^2 = 0.72$) than those with short ice seasons (in-situ duration ≤100 days; $R^2 = 0.52$). The comparative analysis of average yearly ice cover durations between Landsat 8 predictions and observations from Passive Microwave Radiometer (PMR) imagery for 54 lakes ($n = 316$) delivered similar results (Fig. 8b). In general, Landsat 8 overestimated the ice cover durations by about three days and the precision of the predictions increased with longer ice cover durations. The Landsat 8 predictions corresponded better to the ice cover durations that were determined from the first day of freeze up to the last day of break up ($R^2 = 0.85$, MOD = −3 days, RMSE = 23 days) than to the ice cover durations that were determined from the last day of freeze up to the first day of break up ($R^2 = 0.84$, MOD = −20.5 days, RMSE = 28 days).

4. Discussion

We developed the first global-scale LSWT dataset (LakeTEMP) that provides site-specific, quality-controlled observational data for >1.4 million lakes, representing all lakes ≥0.1 km². In addition to curating these data, we standardized the observations into key metrics representing each lake's temperature history for 2013–2021, including the first global-scale compilation of lake-specific ice phenology estimates for every lake ≥0.1 km². This new dataset indicates that across ~1.4 million lakes, the global mean LSWT is 6.3 °C (assuming 0 °C during times of presumed ice cover), and that ~8% of the lakes of the world never freeze, ~6% freeze sporadically, and ~86% freeze every year, corresponding to an estimated proportion of global lake surface area of 23.5%, 19.5%, and 57.0%, respectively. These numbers were not previously available but only speculated about, e.g., by indicating that 'at least 50%' of all lakes are seasonally ice covered (Sharma et al., 2019; Yang et al., 2021). Finally, although only verified for a small number of samples, this work corroborates that artificial lakes, specifically those used for power generation, mining, salt extraction, and aquaculture, are responsible for some of the world's highest LSWTs. This is especially a concern because more natural lakes will be affected by thermal pollution, which has long-lasting effects on lake ecology (Kirillin et al., 2013; Råman Vinnå et al., 2017), as new thermal power plants are being built to meet increased global energy demands (IEA, 2022).

LakeTEMP is intended to enable novel investigations of large-scale thermal lake processes, which to date have focused on the larger lakes of the world. For example, the nine global lake thermal regions proposed by Maberly et al. (2020) were derived from 732 large lakes and could be re-examined with LakeTEMP data that are inclusive of small lakes. Beyond fundamental research applications, this dataset has the potential to serve as baseline calibration or training data for lake models that can simulate historical thermal structures or project future scenarios (e.g., Golub et al., 2022), and can be used to plan lake monitoring programs or to make informed management decisions on lakes with no available data in-situ. Furthermore, the dataset can be easily combined with other large-scale datasets that use the unique lake identifiers from Hydro-LAKES, most notably the LakeATLAS dataset (Lehner et al., 2022), which provides 56 hydro-environmental characteristics for the same ~1.4 million lakes and their lake watersheds. For example, by combining the Aggregated dataset from LakeTEMP and population data from LakeATLAS, we found that of the 965 million people living within 3 km of a lake, the majority lives near an ice-free lake (576 million) or near a lake with sporadic freeze periods (237 million). Another 67 million people live near a lake for which no ice cover duration could be

calculated, but available LSWT data suggest that these might be ice-free as well (i.e., for nearly all lakes the minimum LSWT was >0 °C). The important ecosystem services from lake ice (Knoll et al., 2019) that are provided for the remaining 85 million people living near an annually ice-covered lake, may be increasingly at risk as Sharma et al. (2019) predicted that ~60,000 annually ice-covered lakes will experience ice-free winters given current climate change mitigation trajectories (+3.2 °C).

4.1. Accuracy and uncertainty of data

The validation of LSWT observations with in-situ data produced good results within and some even below the expected range of 1–2 °C RMSE (Lamaro et al., 2013; Simon, 2014; Wloczyk et al., 2006) and trendline estimations of (yearly) mean LSWT were generally accurate within 1.2 °C (based on 95% CIs). However, the validation as well as the comparisons of the mean monthly LSWTs with both the in-situ and the CCI data consistently showed slightly lower measured LSWTs by Landsat 8 (MODs between 0.33 and 0.80 °C). This does not necessarily point to a discrepancy in the dataset but can be explained by the 'cool skin effect' (Hondzo et al., 2022; Wilson et al., 2013), which causes the very thin surface layer from which radiation is measured (<0.1 mm) to be up to 0.8 °C cooler than the layer from which in-situ surface measurements are commonly taken (0.01–1 m). In addition, surfaces that were cooled by passing cloud shadows might have contributed to overall cooler temperatures as measurements taken through cloud edges were retained, whereas the CCI data underwent more extensive cloud removal procedures. This may also explain why differences between Landsat 8 and CCI data were larger in cloudy, northern high-latitude environments.

Although trendlines added a small overall additional bias (MOD) of 0.1 to 0.4 °C to the calculation of mean LSWTs, the observation smoothing improved the overall goodness-of-fit (R^2) by ~0.03 and precision (RMSE) by 0.4 to 0.5 °C. Especially for lakes experiencing recurrent, seasonal high cloud cover, the interpolation of a trendline through those long data gaps inherently corrected for the potential bias in calculating yearly or monthly means from incomplete data. However, when trendlines were fitted through time series of intermittent or ephemeral lakes, faulty predictions were likely made for the seasons when the lake was dry during typically warmer seasons, thus in most cases systematically driving yearly and monthly mean LSWTs higher. As it was not feasible to correct these values directly, a flagging scheme was added to the Aggregated data to indicate the potential level of intermittency for each lake. Another indication of uncertainty provided in the Aggregated data is the number of observations used in the calculation of the summary statistics. By investigating the CIs of all lakes, we found that calculations performed on >85 observations (66.6% of lakes) can be considered reliable (99% of yearly mean LSWT CIs < 1 °C), between 46 and 85 (26.0% of lakes) acceptable (99% of CIs < 2 °C), between 12 and 45 (6.2% of lakes) uncertain (99% of CIs < 7 °C), and between 1 and 11 (0.8% of lakes) insufficient (statistics calculated from observations directly, not from trendline) (Fig. 3).

Traditional lake ice satellite detection methods use either optical or microwave remote sensing techniques (Duguay et al., 2015; Murfitt and Duguay, 2021) and few studies have explored the utility as well as uncertainty of indirect LSWT-based estimations. Zhang et al. (2021) and Nonaka et al. (2007) used Moderate-Resolution Imaging Spectroradiometer (MODIS) daily LSWT data to estimate lake ice phenology and found that the freezing temperature threshold was robust when set between −0.75 °C and 0.5 °C, while the melting temperature should be between 0.5 and 4 °C. As these thresholds are lake-specific and were only tested on 18 lakes, we retained a simple threshold of 0 °C for both freezing and melting processes, hereby potentially introducing a bias towards modelling both 'ice on' and 'ice off' dates too early in the year. A second potential small bias was recognized for the average yearly durations of ice cover, which were, compared to both in-situ and passive microwave radiometer measurements, in general overestimated by

about three to six days. However, these inaccuracies are defined based on either in-situ observations, or on visible wavelengths observed from space, which both have their own limitations and uncertainties. Most notably, the definitions for the 'ice on' moment can vary from using the onset of ice formation, a percentage of ice cover, to whole lake freeze up; and the definitions for the 'ice off' moment can vary from using the first sign of break up, the start of boats being able to navigate, to complete ice free waters. This can introduce differences in total ice cover duration in the order of weeks (Cai et al., 2022; Sharma et al., 2022). In addition, the discussed bias of Landsat 8 derived LSWT observations towards under-estimating real temperatures may exacerbate the overestimation of ice cover duration by introducing faulty $\leq 0\,°C$ data points. Finally, short ice cover durations (≤ 100 days) have a larger uncertainty than long dura-tions, which could point to higher interannual variability when forcing variables (e.g., air temperature, wind) are near the thresholds for freezing conditions.

4.2. Limitations in data usage

The LakeTEMP dataset is intended for use within large-scale (regional to global) analyses, rather than lake-specific or local-scale studies. The presented global maps and performed statistical tests confirm an accurate representation of LSWTs of lake regions and larger geographies; however, the automated quality control methods used in this work do not warrant correct results for all individual lakes. Spe-cifically, noisy data can have passed *Z-score* filtering, or observations taken from dry lake beds might not have been detected (i.e., the land cover classification was not accurate) and therefore not removed. In addition to spatial constraints, the presented dataset shows some limi-tations due to its temporal resolution and covered timespan. We there-fore believe that the data are best used for studies seeking to understand current thermal functioning of global lakes, or the roles that lakes currently play in other large-scale processes (e.g., ecological, biogeo-chemical, climatological), but are less adequate for studies focusing on temporal changes and thermal shifts associated with anthropogenic stressors or climate change. We also want to emphasize that this work describes average LSWT conditions and that investigations into extreme events using the observational data might not be suitable as statistically important high or low temperatures may not have been recorded. We encourage data users to complement the LakeTEMP dataset with other available global LSWT and ice cover datasets (e.g., Cai et al., 2021, 2022; Carrea et al., 2022, 2023) that can provide higher-frequency data for large-sized lakes.

We caution data users that the observations provided by LakeTEMP refer to the thermal conditions of lakes at their center point, whereas lake thermal processes are known to be affected by intralake heteroge-neity (Mason et al., 2016; Woolway and Merchant, 2018), especially between shallower and deeper sections of medium to large sized lakes. Furthermore, negative LSWT observations taken from saline lakes could reflect unfrozen conditions and trendline predictions might therefore have overestimated the ice cover durations for those specific lakes. Finally, we did not provide LSWT observations for lakes smaller than 0.1 km^2, which is the size limit set by the underpinning lake delineations offered in the HydroLAKES database. Although the GLAKES database includes lakes as small as 0.03 km^2 (Pi et al., 2022), we did not make use of these polygons because of the increased risk of central Landsat 8 pixels representing mixed water-land surfaces, and because of the increased risk that a polygon belongs to a non-lake feature, such as a river section, which is indicated as a limitation in the GLAKES docu-mentation. Therefore, we urge data users to consider the potential biases introduced by the lack of representation of very small lakes and ponds (<0.1 km^2), for example the accelerated rates of heat exchanges in small lakes (Woolway et al., 2017).

4.3. Continuation of dataset

Upon its launch in 2013, Landsat 8 had a design life of five years but was expected to last over ten years. Anno 2024 it is still in orbit and in 2021, Landsat 9 was launched. This satellite has a similar design to Landsat 8 and we expect that the same workflows can be used to extend the LakeTEMP dataset into the future, enabling the analysis of long-term trends in global LSWT. The USGS released Landsat Collection 2 after the data used for this study (i.e., from Collection 1) were downloaded, post-processed and analyzed. Although data quality of Collection 1 is still warranted, the improved data processing and access capabilities of Collection 2 have the potential to further advance the workflow and quality of the datasets presented in this study.

5. Conclusions

Global-scale LSWT data are needed to understand the Earth's aquatic cycle, including the role of lakes as climate sentinels, biodiversity hab-itats, and providers of diverse services to humans. Here, we presented surface water temperature observations for all lakes in the world that have a surface area of at least 0.1 km^2 ($\sim$1.4 million lakes) and summary statistics interpolated from these observations, including ice phenology estimations. This is the first LSWT dataset that provides site specific and quality-controlled data at such a large scope, thereby filling a crucial spatial gap for the incorporation of small lakes and understudied ge-ographies of remote regions. The LakeTEMP dataset is freely available and offered in a ready-to-analyze format, to foster smooth applications to further research.

CRediT authorship contribution statement

Maartje C. Korver: Conceptualization, Formal analysis, Investiga-tion, Methodology, Software, Validation, Visualization, Writing – orig-inal draft. **Bernhard Lehner:** Conceptualization, Funding acquisition, Supervision, Writing – review & editing. **Jeffrey A. Cardille:** Concep-tualization, Resources, Writing – review & editing. **Laura Carrea:** Validation, Writing – review & editing.

Declaration of competing interest

The authors declare that they have no known competing financial interests or personal relationships that could have appeared to influence the work reported in this paper.

Data availability

The LakeTEMP dataset is publicly available under a CC-BY-4.0 Li-cense at the following URL: https://doi.org/10.6084/m9. figshare.23844660 (Korver et al., 2024).

Appendices

A.1. Calculation of lake center points

Lake shoreline polygons were converted to grid format (cell size of 0.0003°, i.e., ~30 m at the equator), setting the grid cells inside the lake to 'Null' and the grid cells outside the lake to '0'. Then, a geodesic distance to the nearest '0' value was calculated for every 'Null' raster cell. For every lake, its maximum distance value was identified by using zonal statistics, and within each lake the cell matching this distance was extracted using map algebra. These 'maximum distance' cells were then converted to lake center points (Fig. A.1). Following this procedure, some lakes contained more than one center point, in which case one of the points was randomly selected. All calculations were performed in the Geographic Information System ArcGIS version 10.7.1.
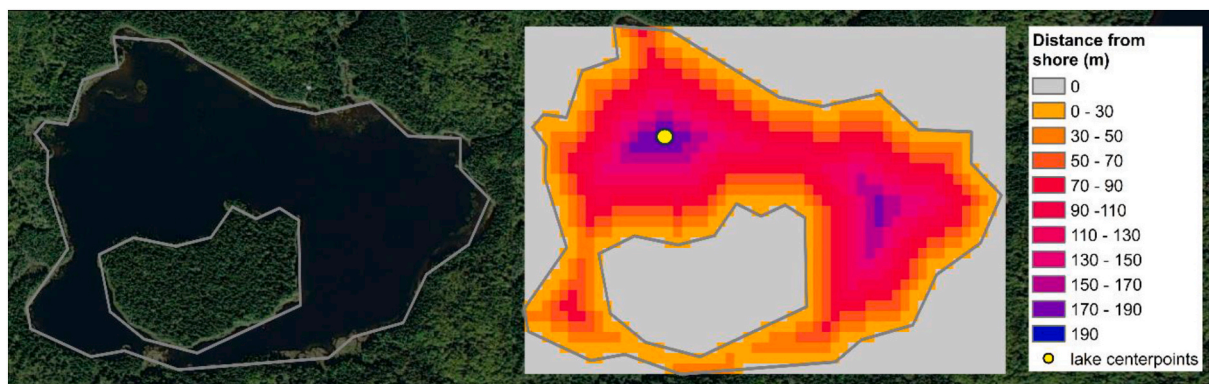
Fig. A.1. Example of the calculation of a lake center point, using the furthest distance from any lake shore or island.

A.2. In-situ validation of Landsat 8 lake surface water temperature

LSWT observations were validated against in-situ observations from 48 lakes across 5 continents, of which 13 large lakes provided data for multiple sites thus representing 63 sites in total. Table A.1 provides the metadata and Table A.2 provides the validation results for each lake. In addition, we analyzed the effects of using 1) a Single Channel (SC) instead of a Split-Window (SW) algorithm and 2) Landsat 7 in addition to Landsat 8 observations, by repeating the in-situ validation on these respective datasets (Table A.2).

Table A.1

Metadata of the in-situ locations used for validation of Landsat 8 LSWT observations, including lake name, country, lake area, and 'Hylak_id' (unique identifier corresponding to the HydroLAKES dataset (Messager et al., 2016)), the observation frequency and depth below the surface of the in-situ temperature sensors, and where available, the citation of the in-situ source data.

Lake name	Country	Hylak id	Lake area (km^2)	Observation frequency	Sensor depth	Citation
Wivenhoe	Australia	1660	103	Hourly	< 1	
Carioca	Brazil	1,098,524	0.1	Hourly	0.5	Barbosa et al. (2004)
892	Canada	921,275	0.1	Hourly	1.0	Desmarais et al. (2020)
Bates	Canada	4678	20	Hourly	2.0	
Kathleen	Canada	4545	34	Hourly	1.5	
Mush	Canada	4645	18	Hourly	2.0	
Erie	Canada	9	25,768	Hourly	1.0	
Erie	Canada	9	25,768	Hourly	1.0	
Nipissing	Canada	745	878	Hourly	na	
Nipissing	Canada	745	878	Hourly	1.0	
Ontario	Canada	7	19,347	Hourly	0.6	
Ontario	Canada	7	19,347	Hourly	0.6	
Saint Clair	Canada	66	1161	Hourly	na	
Simcoe	Canada	759	767	Hourly	na	
Winnipeg	Canada	4	23,923	Hourly	na	
Winnipeg	Canada	4	23,923	Hourly	na	
Woods	Canada	57	3473	Hourly	na	
Huron	Canada USA	8	59,399	Hourly	1.0	
Huron	Canada USA	8	59,399	Hourly	1.0	
Great Slave	Canada	3	26,734	Hourly	na	
Great Slave	Canada	3	26,734	Hourly	na	
Gullchuk	Canada	906,851	0.5	Hourly	1.0	
Namu	Canada	94,103	3.2	Hourly	1.0	
Lhù'ààn Mân' Brooks	Canada	363	398	Hourly	2.5	McKnight (2022)
Lhù'ààn Mân' Deep	Canada	363	398	Hourly	2.5	McKnight (2022)
Lhù'ààn Mân' South	Canada	363	398	Hourly	2.5	McKnight (2022)
Lhù'ààn Mân' Talbot	Canada	363	398	Hourly	2.5	McKnight (2022)
Superior	Canada USA	5	81,844	Hourly	1.0	
Superior	Canada USA	5	81,844	Hourly	1.0	
Vorstjarv	Estonia	1164	260	Hourly	0.5	
Vorstjarv	Estonia	1164	260	Hourly	1.0	
Kulovesi	Finland	12,545	86	Daily**	1.0	
Lestijarvi	Finland	12,141	64	Daily**	1.0	
Pyhajarvi	Finland	1137	122	Daily**	1.0	
Yli-Kitka	Finland	1067	289	Daily**	1.0	
Lough Feeagh	Ireland	163,604	3.8	Hourly	0.9	de Eyto et al. (2020)
Garda	Italy	1282	355	Daily**	0.5	
Iseo	Italy	14,185	59	Daily**	1.0	
Maggiore	Italy	1275	208	Daily**	0.5	
Qaraoun Q6	Lebanon	174,944	5.5	Daily***	0.2	
Qaraoun Q9	Lebanon	174,944	5.5	Daily***	0.2	
Kivu	Rwanda	163	2700	Daily*	0.5	Descy and Guillard (2014)
Malaren	Sweden	102	1083	Daily*	0.5	Miljödata (2023)
Erken	Sweden	12,809	23	Hourly	1.0	
Windermere	UK	13,387	13	Hourly	1.0	Jones et al. (2017)
Mendota	USA	9086	41	Hourly	0	Magnuson et al. (2023)
Barco	USA	na	na	Hourly	0.1	National Ecological Observatory Network (NEON) (2021)
Little Rock	USA	1,032,416	0.1	Hourly	0.1	National Ecological Observatory Network (NEON) (2021)
Suggs	USA	1,066,600	0.3	Hourly	0.1	National Ecological Observatory Network (NEON) (2021)
Crampton	USA	1,029,915	0.2	Hourly	0.1	National Ecological Observatory Network (NEON) (2021)
Champlain	USA	64	1141	Hourly	1.0	
Champlain	USA	64	1141	Hourly	1.0	
Douglas	USA	8817	15	Hourly	1.0	
George	USA	767	113	Hourly	0.8–1.2	Kolar et al. (2021); Lucius et al. (2022a, 2022b)
Lillinonah	USA	na	na	Hourly	0.6	Klug et al. (2021)
Sunapee	USA	9068	16	Hourly	1.5	LSPA, Weathers, K.C., and Steele, B.G (2021)
Trout	USA	8736	15	Hourly	0	Lead et al. (2020)
Mead	USA	809	581	Hourly	0.5	
Mead	USA	809	581	Hourly	0.5	
Mohave	USA	9360	99	Hourly	0.5	
St. John River	USA	na	na	Hourly	na	
Michigan	USA	6	57,727	Hourly	1.0	
Michigan	USA	6	57,727	Hourly	0.6	

* = Daily average.
** = Daily instantaneous.
*** = Synchronous with Landsat overpass.

Table A.2

Validation of LSWT observations with in-situ data. Results are shown for Landsat 8 observations of the Primary dataset that are processed with a split-window (SW) algorithm (Jiménez-Muñoz et al., 2014), for Landsat 8 data processed with a single-channel (SC) algorithm (Jiménez-Muñoz et al., 2009), and for a combination of Landsat 7 (SC with atmospheric corrections from TIGR61 database) and Landsat 8 (SW) observations. Lake metadata can be found in Table A.1. Validation results include the R^2 of a linear regression between Landsat and in-situ observations, the root mean square error (RMSE) and median of differences (MOD) of the observation differences (in-situ LSWT minus Landsat LSWT), and the number of observations (n) used in each validation.

Lake name	L8 – SW R^2	RMSE (°C)	MOD (°C)	n	L8 – SC R^2	RMSE (°C)	MOD (°C)	n*	Combined L7 and L8 R^2	RMSE (°C)	MOD (°C)	n
Wivenhoe	0.96	0.72	0.3	21	0.85	1.61	0.2	24	0.91	1.22	−0.4	47
Carioca	0.92	1.07	2.2	21	0.61	2.22	1.1	21	0.71	1.75	1.1	44
892	0.82	2.84	1.9	29	0.75	3.02	0.6	29	0.88	2.11	0.8	49
Bates	0.67	1.64	0.1	28	0.3	2.35	0.3	29	0.45	1.82	−0.1	51
Kathleen	0.66	1.23	0.3	31	0.47	1.39	0.2	32	0.62	1.18	0.0	53
Mush	0.71	1.22	0.0	27	0.48	1.41	−0.4	26	0.42	1.65	−0.4	46
Erie	0.81	1.75	0.6	61	0.65	2.26	0.9	59	0.77	1.75	0.4	116
Erie	0.87	1.31	1.0	27	0.57	2.31	1.1	27	0.74	1.67	0.8	49
Nipissing	0.89	1.34	0.7	46	0.6	2.32	0.5	42	0.78	1.92	0.2	73
Nipissing	0.8	1.67	0.9	46	0.77	1.81	0.5	46	0.66	2.28	0.3	89
Ontario	0.98	1.04	0.6	88	0.87	2.4	1.1	89	0.92	1.85	0.3	148
Ontario	0.83	2.30	1.0	78	0.66	3.22	0.7	79	0.8	2.40	0.3	135
Saint Clair	0.94	1.15	0.5	45	0.81	2.13	0.8	43	0.83	2.13	0.2	79
Simcoe	0.81	1.51	1.0	30	0.33	2.64	1.5	28	0.68	2.14	0.6	55
Winnipeg	0.93	1.17	0.3	43	0.82	1.95	1.0	37	0.78	2.02	0.2	69
Winnipeg	0.76	1.79	−0.1	19	0.55	2.67	0.3	17	0.69	1.95	0.0	30
Woods	0.72	1.86	0.2	35	0.6	2.46	0.5	33	0.59	2.58	−0.2	58
Huron	0.95	1.21	0.8	67	0.84	2.25	0.6	68	0.85	2.13	0.6	119
Huron	0.93	1.69	0.6	39	0.78	2.87	0.8	39	0.84	2.28	0.4	70
Great Slave	0.95	0.80	0.1	25	0.73	1.74	0.7	24	0.81	1.48	0.5	51
Great Slave	0.93	0.85	0.3	22	0.79	1.42	0.6	19	0.76	1.53	0.4	35
Gullchuk	0.94	1.44	0.9	40	0.81	2.43	−0.5	52	0.82	2.46	−0.2	92
Namu	0.89	2.09	0.3	27	0.76	2.82	2.3	19	0.88	1.97	1.5	46
Lhù'ààn Mân' Brooks	0.75	2.33	1.2	32	0.71	2.50	0.5	32	0.77	2.19	0.7	58
Lhù'ààn Mân' Deep	0.96	0.72	0.8	22	0.91	1.10	0.1	22	0.84	1.48	0.1	39
Lhù'ààn Mân' South	0.77	1.61	0.6	19	0.7	1.82	0.3	19	0.69	1.61	0.6	35
Lhù'ààn Mân' Talbot	0.9	1.55	1.1	12	0.77	2.34	0.6	13	0.91	1.38	0.6	25
Superior	0.91	1.48	0.6	58	0.81	2.14	0.5	59	0.91	1.47	0.3	103
Superior	0.92	1.19	0.2	67	0.83	1.84	0.3	67	0.84	1.79	0.0	112
Vorstjarv	0.94	1.69	0.7	58	0.92	1.99	0.5	58	0.93	1.68	0.2	105
Vorstjarv	0.91	1.81	0.4	52	0.86	2.23	0.7	53	0.89	1.83	0.1	85
Kulovesi	0.99	0.81	1.2	6	0.99	0.93	0.6	6	0.99	0.81	1.0	7
Lestijarvi	0.94	2.13	−1.1	3	0.99	0.73	1.4	3	0.94	1.92	−0.1	4
Pyhajarvi	0.82	2.61	1.4	5	0.59	3.89	3.0	5	0.84	1.92	1.1	8
Yli-Kitka	0.19	1.72	−0.5	3	0.03	1.88	2.1	3	0.88	1.22	0.4	4
Lough Feeagh	0.84	1.83	0.8	43	0.75	2.24	1.1	43	0.81	1.81	1.0	62
Garda	0.93	1.57	0.6	5	0.93	1.64	0.3	5	0.90	2.09	0.2	12
Iseo	0.97	1.05	0.6	32	0.96	1.23	−0.1	32	0.97	1.05	0.6	32
Maggiore	0.96	1.09	−0.7	7	0.94	1.27	0.0	7	0.96	1.08	−0.6	10
Qaraoun Q6	0.99	0.84	−0.8	9	0.98	0.90	−2.5	9	0.95	1.35	−1.3	18
Qaraoun Q9	0.95	1.69	−0.9	11	0.95	1.65	−2.9	11	0.93	1.57	−1.9	18
Kivu	0.11	0.55	0.4	8	0.06	0.56	6.3	8	0.19	0.58	0.7	14
Malaren	1	0.62	0.5	4	0.94	2.62	2.4	4	1.00	0.62	0.4	5
Erken	0.95	1.49	0.7	146	0.9	2.12	0.6	144	0.93	1.69	0.3	232
Windermere	0.98	0.82	−0.4	14	0.94	1.39	0.7	14	0.92	1.52	−0.5	24
Mendota	0.89	2.23	0.4	37	0.84	2.53	0.4	38	0.88	2.02	−0.1	68
Barco	0.83	2.07	0.5	37	0.55	3.38	0.6	32	0.50	3.60	0.4	60
Little Rock	0.97	1.31	0.3	7	0.93	1.70	0.1	8	0.77	2.16	0.4	22
Suggs	0.89	1.81	0.6	33	0.59	3.19	0.7	33	0.70	2.80	−0.1	66
Crampton	0.94	1.48	−0.6	19	0.91	1.74	0.1	19	0.87	2.07	0.0	39
Champlain	0.94	1.10	0.9	16	0.83	1.61	1.1	15	0.91	1.13	0.2	26
Champlain	0.89	1.21	0.5	21	0.73	1.94	0.6	21	0.75	1.74	0.3	40
Douglas	0.92	1.25	0.6	64	0.71	2.43	1.5	63	0.70	2.32	0.9	111
George	0.95	1.14	0.7	14	0.81	2.63	0.9	15	0.80	2.52	0.8	25
Lillinonah	0.84	1.05	1.9	11	0.34	1.87	1.2	11	0.38	2.03	1.0	23
Sunapee	0.44	2.02	0.5	10	0.03	2.70	0.8	10	0.52	2.44	0.0	22
Trout	0.99	0.67	1.0	10	0.93	1.59	0.2	10	0.75	2.25	0.0	33
Mead	0.98	0.71	0.9	42	0.96	1.04	0.1	42	0.94	1.41	0.8	81
Mead	0.98	0.81	0.9	43	0.96	1.15	−0.2	43	0.95	1.37	0.5	83
Mohave	0.95	1.49	0.6	41	0.94	1.56	−0.6	41	0.96	1.33	0.4	87
St. John River	0.89	1.50	0.9	43	0.65	2.66	1.6	42	0.86	1.68	0.4	68
Michigan	0.93	1.47	0.4	64	0.86	2.07	0.3	68	0.88	1.99	0.1	125
Michigan	0.95	1.24	0.2	66	0.83	2.24	0.3	67	0.92	1.62	0.0	123
All	**0.94**	**1.71**	**0.4**	**2074**	**0.86**	**2.50**	**0.6**	**2077**	**0.89**	**2.15**	**0.3**	**3718**

* Differences in the number of observations in L8 – SW results are explained by slight differences in data filtering (i.e., outlier detection and removal of LSWT <0 °C).

A.3. Extraction of water occurrence data at lake center locations

The Global Surface Water (GSW) dataset of the European Commission's Joint research Centre (Pekel et al., 2016) provides the global occurrence of inland water surfaces between 1984 and 2021 in multiple raster-based mapping products. The GSW Monthly Water History (v1.3) product contains monthly raster files with a 'water', 'no water' (hereon referred to as 'land'), 'unknown', or 'not available' (NA) class for every 0.9 arc-second pixel (~30 m at the equator) of the global land surface, where frozen water surfaces fall under the 'unknown' class. For every month between 2013 and 2021 and every lake, all class values were extracted that occurred within the same 50 m × 50 m square buffer around the lake center point as used for LSWT calculations. From the set of extracted pixels a single flag was defined as follows: 1) 'water' if the number of water pixels exceeded the number of land pixels; and 'land' if the number of land pixels was equal to or exceeded the number of water pixels, both irrespective of the number of unknown values; 2) 'unknown' if only unknown class values were represented; 3) 'land' if only unknown class values were represented, but LSWT exceeded 40 °C indicating a high likelihood of representing a land value; and 4) 'no information' if all pixels were NA. Table A.3 shows the percent occurrence of each flag in the Primary dataset, specified by the different combinations of pixel classes from which the flags were derived. In total, 6.8% of LSWT observations were flagged based on a mixture of land, water, and in some cases unknown pixels. For about two-thirds of these observations, the flags were assigned based on a clear majority of either land or water pixels (i.e., more than twice in number).

Table A.3
The fraction of LSWT observations flagged as 'water', 'land', 'unknown', or 'no information', specified by the different combinations of pixel values from which the flags were derived.

Flag and pixel value conditions	Fraction of observations in Primary dataset (%)
No information	
not available	1.0
Unknown	
unknown	46.9
Land	
unknown and > 40 °C	<0.1
land	5.2
land; unknown	0.5
land ≥ water	1.4
land ≥ water; unknown	0.2
Water	
water	40.1
water; unknown	0.0
water > land	2.4
water > land; unknown	2.3

A.4. Seasonal trendlines

Seasonal trendlines were generated in R, using a Generalized Additive Model (GAM) ('mgcv' package version 1.8–42, https://CRAN.R-project.org/package=mgcv), an additive modelling technique that uses smooth functions to predict non-linear regression trends (Wood, 2017). Trendlines were calculated for each Julian day, while leap years were ignored by matching observations taken on February 29 to Julian day 59 (February 28). To ensure that the seasonal trend was cyclic (i.e., the trendline at Julian day 365 transitions smoothly into Julian day 1), each GAM was plotted through the original and a duplicate timeseries (creating a 720-day timeseries). Then, the first 152 days and the last 204 days were removed to obtain a 365-day model. This approach was preferred to using a 'cyclic cubic spline', as the latter introduced extrapolation issues when data gaps were present towards the start or the end of year. The number of knots, which is a setting affecting the smoothness of the trendline, is usually selected by visual inspection of the plot. However, due to the large number of GAM models to plot (i.e., >1.4 million), one constant value was chosen (k = 12) based on visual inspections of trendlines applied to the timeseries of lakes that were part of the in-situ validation and comparison analyses. As a result, GAM models could not be calculated for timeseries with <12 observations.

A.5. Distribution of yearly average LSWTs
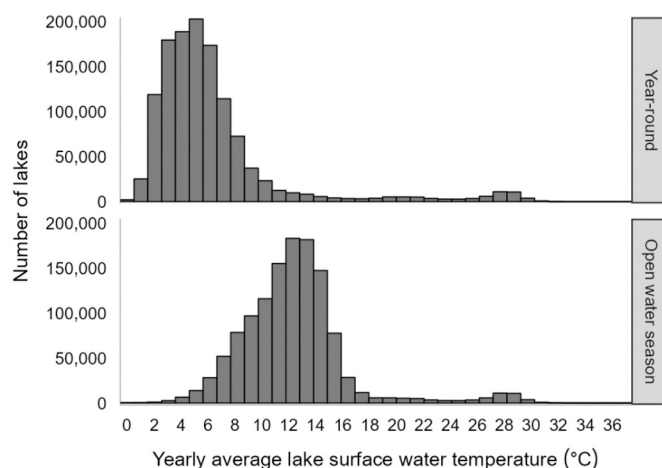
Fig. A.2. Histogram of yearly average lake surface water temperatures (°C) for all lakes excluding the 179,524 lakes that were flagged for potential intermittency (levels 1 to 4, Table 1) and the 11,437 lakes with <12 LSWT observations. Averages were calculated from the 365 daily trendline values, assuming 0 °C during times of presumed ice cover (upper panel, 'Year-round'), and from trendline values >0 °C only (lower panel, 'Open water season').

References

Adrian, R., O'Reilly, C.M., Zagarese, H., Baines, S.B., Hessen, D.O., Keller, W., Livingstone, D.M., Sommaruga, R., Straile, D., Van Donk, E., Weyhenmeyer, G.A., Winder, M., 2009. Lakes as sentinels of climate change. Limnol. Oceanogr. 54, 2283–2297. https://doi.org/10.4319/lo.2009.54.6_part_2.2283.

Attiah, G., Kheyrollah Pour, H., Scott, K.A., 2023. Lake surface temperature retrieved from Landsat satellite series (1984 to 2021) for the North slave region. Earth Syst. Sci. Data 15 (3), 1329–1355. https://doi.org/10.5194/essd-15-1329-2023.

Balsamo, G., Salgado, R., Dutra, E., Boussetta, S., Stockdale, T., Potes, M., 2012. On the contribution of lakes in predicting near-surface temperature in a global weather forecasting model. Tellus A: Dynam. Meteorol. Oceanography 64 (1), 15829. https://doi.org/10.3402/tellusa.v64i0.15829.

Barbosa, F.A.R., Scarano, F.R., Sabará, M.G., Esteves, F.A., 2004. Brazilian LTER: ecosystem and biodiversity information in support of decision-making. Environ. Monit. Assess. 90 (1–3), 121–133. https://doi.org/10.1023/b:emas.0000003571.10570.02.

Benson, B., Magnuson, J., Sharma, S., 2000, updated 2020. Global Lake and River Ice Phenology Database, Version 1. [Subset: 'Lake Only']. Boulder, Colorado USA. NSIDC: National Snow and Ice Data Center. https://doi.org/10.7265/N5W66HP8 [Date Accessed: 2023-02-07] [dataset].

Brown, L.C., Duguay, C.R., 2010. The response and role of ice cover in lake-climate interactions. Progress Phys. Geography: Earth Environ. 34 (5), 671–704. https://doi.org/10.1177/0309133310375653.

Cai, Yu, Duguay, Claude R., Ke, Chang-Qing, 2021. Lake ice Phenology in the Northern Hemisphere Extracted from SMMR, SSM/I and SSMIS Data from 1979 to 2020. PANGAEA. https://doi.org/10.1594/PANGAEA.937904 [Date accessed: 2023-02-07] [dataset].

Cai, Y., Duguay, C.R., Ke, C.-Q., 2022. A 41-year (1979–2019) passive-microwave-derived lake ice phenology data record of the northern hemisphere. Earth Syst. Sci. Data 14 (7), 3329–3347. https://doi.org/10.5194/essd-14-3329-2022.

Carrea, L., Embury, O., Merchant, C.J., 2015. Datasets related to in-land water for limnology and remote sensing applications: distance-to-land, distance-to-water, water-body identifier and Lake-Centre co-ordinates. Geosci. Data J. 2 (2), 83–97. https://doi.org/10.1002/gdj3.32.

Carrea, L., Crétaux, J.-F., Liu, X., Wu, Y., Bergé-Nguyen, M., Calmettes, B., Duguay, C., Jiang, D., Merchant, C.J., Mueller, D., Selmes, N., Spyrakos, E., Simis, S., Stelzer, K., Warren, M., Yesou, H., Zhang, D., 2022. ESA Lakes Climate Change Initiative (Lakes_cci): Lake Products, Version 2.0. NERC EDS Centre for Environmental Data Analysis. https://doi.org/10.5285/ab8d21568c81491fbb9a300c36884af7 [Date accessed: 2021-11-19] [dataset].

Carrea, L., Crétaux, J.-F., Liu, X., Wu, Y., Calmettes, B., Duguay, C.R., Merchant, C.J., Selmes, N., Simis, S.G.H., Warren, M., Yesou, H., Müller, D., Jiang, D., Embury, O., Bergé-Nguyen, M., Albergel, C., 2023. Satellite-derived multivariate world-wide lake physical variable timeseries for climate studies. Sci. Data 10 (1). https://doi.org/10.1038/s41597-022-01889-z.

de Eyto, E., Dillane, M., Moore, T., Wilson, H., Cooney, J., Hughes, P., Murphy, M., Nixon, P., Sweeney, D., Poole, R., 2020. Lough Feeagh water Temperature Profiles (Version 1). Marine Institute, Ireland. https://doi.org/10.20393/91ff84cc-a10d-45d0-9b30-e2d11a040e95 [Date accessed: 2020-08-25] [dataset].

Descy, J.P., Guillard, J., 2014. Biological Baseline of Lake Kivu: Final Report. Université de Namur & Carrtel, p. 33. Data available online at: https://www.uvm.edu/femc/data/archive/project/geisha-stormblitzfr/dataset/kivu-daily-high-frequency-lake-data [Date accessed: 2021-09-05] [dataset].

Desmarais, I., White, R., Haughton, E., Korver, M., Tank, S.E., Giesbrecht, I.J.W., 2020. Baseline limnology of lakes in the Kwakshua watersheds of Calvert and Hecate

Islands, BC: 2016-2019. Version 2.0. Hakai Institute Data Package. https://doi.org/10.21966/q2tr-2n80 [Date accessed: 2020-05-01] [dataset].

Dombrovsky, L.A., Kokhanovsky, A.A., 2023. Solar heating of ice-covered lake and ice melting. J. Quant. Spectrosc. Radiat. Transf. 294, 108391 https://doi.org/10.1016/j.jqsrt.2022.108391.

Downing, J.A., 2009. Global limnology: up-scaling aquatic services and processes to planet Earth. In: SIL Proceedings, 1922–2010, 30:8, pp. 1149–1166. https://doi.org/10.1080/03680770.2009.11923903.

Du, J., Kimball, J.S., 2018. Daily Lake Ice Phenology Time Series Derived from AMSR-E and AMSR2, Version 1. NASA National Snow and Ice Data Center Distributed Active Archive Center, Boulder, Colorado USA. https://doi.org/10.5067/HT4NQO7ZJF7M [Date accessed: 2023-08-02] [dataset].

Du, C., Ren, H., Qin, Q., Meng, J., Zhao, S., 2015. A practical Split-window algorithm for estimating land surface temperature from Landsat 8 data. Remote Sens. 7 (1), 647–665. https://doi.org/10.3390/rs70100647.

Duguay, C.R., Bernier, M., Gauthier, Y., Kouraev, A., 2015. Remote sensing of lake and river ice. In: Remote Sensing of the Cryosphere. John Wiley & Sons, Ltd., pp. 273–306. https://doi.org/10.1002/9781118368909.ch12

Edinger, J.E., Duttweiler, D.W., Geyer, J.C., 1968. The response of water temperatures to meteorological conditions. Water Resour. Res. 4 (5), 1137–1143. https://doi.org/10.1029/WR004i005p01137.

Ermida, S.L., Soares, P., Mantas, V., Göttsche, F.-M., Trigo, I.F., 2020. Google Earth Engine Open-Source Code for Land Surface Temperature Estimation from the Landsat Series. Remote Sens. 12, 1471. https://doi.org/10.3390/rs12091471.

Giroux-Bougard, X., Fluet-Chouinard, E., Crowley, M.A., Cardille, J.A., Humphries, M.M., 2023. Multi-sensor detection of spring breakup phenology of Canada's lakes. Remote Sens. Environ. 295, 113656. https://doi.org/10.1016/j.rse.2023.113656.

Golub, M., Thiery, W., Marcé, R., Pierson, D., Vanderkelen, I., Mercado-Bettin, D., Woolway, R.I., Grant, L., Jennings, E., Kraemer, B.M., Schewe, J., Zhao, F., Frieler, K., Mengel, M., Bogomolov, V.Y., Bouffard, D., Côté, M., Couture, R.-M., Debolskiy, A.V., Zdorovennova, G., 2022. A framework for ensemble modelling of climate change impacts on lakes worldwide: the ISIMIP Lake sector. Geosci. Model Dev. 15 (11), 4597–4623. https://doi.org/10.5194/gmd-15-4597-2022.

Hair, J.F., Black, W.C., Babin, B.J., Anderson, R.E., 2010. Multivariate Data Analysis, 7th edition. Pearson, New York.

Heino, J., Alahuhta, J., Bini, L.M., Cai, Y., Heiskanen, A.-S., Hellsten, S., Kortelainen, P., Kotamäki, N., Tolonen, K.T., Vihervaara, P., Vilmi, A., Angeler, D.G., 2021. Lakes in the era of global change: moving beyond single-lake thinking in maintaining biodiversity and ecosystem services. Biol. Rev. 96 (1), 89–106. https://doi.org/10.1111/brv.12647.

Hondzo, M., You, J., Taylor, J., Bartlet, G., Voller, V.R., 2022. Measurement and scaling of lake surface skin temperatures. Geophys. Res. Lett. 49 https://doi.org/10.1029/2021GL093226.

IEA, 2022. World Energy Outlook 2022. IEA, Paris. https://www.iea.org/reports/world-energy-outlook-2022.

Jane, S.F., Hansen, G.J.A., Kraemer, B.M., Leavitt, P.R., Mincer, J.L., North, R.L., Pilla, R.M., Stetler, J.T., Williamson, C.E., Woolway, R.I., Arvola, L., Chandra, S., DeGasperi, C.L., Diemer, L., Dunalska, J., Erina, O., Flaim, G., Grossart, H.-P., Hambright, K.D., Rose, K.C., 2021. Widespread deoxygenation of temperate lakes. Nature 594 (7861). https://doi.org/10.1038/s41586-021-03550-y.

Jansen, J., Woolway, R.I., Kraemer, B.M., Albergel, C., Bastviken, D., Weyhenmeyer, G.A., Marcé, R., Sharma, S., Sobek, S., Tranvik, L.J., Perroud, M., Golub, M., Moore, T.N., Råman Vinnå, L., La Fuente, S., Grant, L., Pierson, D.C., Thiery, W., Jennings, E., 2022. Global increase in methane production under future warming of lake bottom waters. Glob. Chang. Biol. 28 (18), 5427–5440. https://doi.org/10.1111/gcb.16298.

Janssen, A.B.G., Hilt, S., Kosten, S., Klein, J.J.M., Paerl, H.W., Van de Waal, D.B., 2021. Shifting states, shifting services: linking regime shifts to changes in ecosystem

services of shallow lakes. Freshw. Biol. 66 (1), 1–12. https://doi.org/10.1111/fwb.13582.

Jiménez-Muñoz, J.C., Cristobal, J., Sobrino, J.A., Soria, G., Ninyerola, M., Pons, X., Pons, X., 2009. Revision of the Single-Channel algorithm for land surface temperature retrieval from Landsat thermal-infrared data. IEEE Trans. Geosci. Remote Sens. 47 (1), 339–349. https://doi.org/10.1109/TGRS.2008.2007125.

Jiménez-Muñoz, J.C., Sobrino, J.A., Skokovic, D., Mattar, C., Cristobal, J., 2014. Land surface temperature retrieval methods from Landsat-8 thermal infrared sensor data. IEEE Geosci. Remote Sens. Lett. 11 (10), 1840–1843. https://doi.org/10.1109/LGRS.2014.2312032.

Jones, I.D., Feuchtmayr, H., Maberly, S.C., 2017. Data from automatic water monitoring buoy from Windermere south basin, 2012 to 2015. NERC Environmental Information Data Centre. https://doi.org/10.5285/e68063b9-2e52-44df-8b6f-a3deb37b76cb [Date accessed: 2021-01-28] [dataset].

Kalnay, E., Kanamitsu, M., Kistler, R., Collins, W., Deaven, D., Gandin, L., Iredell, M., Saha, S., White, G., Woollen, J., Zhu, Y., Chelliah, M., Ebisuzaki, W., Higgins, W., Janowiak, J., Mo, K.C., Ropelewski, C., Wang, J., Leetmaa, A., Joseph, D., 1996. The NCEP/NCAR 40-year reanalysis project. Bull. Am. Meteorol. Soc. 77 (3), 437–472. https://doi.org/10.1175/1520-0477(1996)077<0437:TNYRP\>2.0.CO;2.

Kirillin, G., Shatwell, T., Kasprzak, P., 2013. Consequences of thermal pollution from a nuclear plant on lake temperature and mixing regime. J. Hydrol. 496, 47–56. https://doi.org/10.1016/j.jhydrol.2013.05.023.

Klug, J.L., White, R., Bollard, G., 2021. High-Frequency Water Temperature Data at Lake Lillinonah, Connecticut, USA, 2018-current ver 3. Environmental Data Initiative. https://doi.org/10.6073/pasta/aa52d634823599b490d6fcf8dd24f490 [Date accessed: 2021-12-02] [dataset].

Knoll, L.B., Sharma, S., Denfeld, B.A., Flaim, G., Hori, Y., Magnuson, J.J., Straile, D., Weyhenmeyer, G.A., 2019. Consequences of lake and river ice loss on cultural ecosystem services. Limnol. Oceanography Lett. 4 (5), 119–131. https://doi.org/10.1002/lol2.10116.

Kolar, H.R., Eichler, L.W., Lucius, M.A., Moriarty, V.W., Corbiere, M.M., Kelly, M.R., Mapara, M.I., 2021. The Jefferson Project 2017 Water Quality Data from Two Vertical Profiler Stations in Lake. ver 1. Environmental Data Initiative, George, NY, USA. https://doi.org/10.6073/pasta/1ea03a273bb7dd2e3b1131a837c55b86 [Date accessed: 2021-12-02] [dataset].

Korver, Maartje C., Cardille, Jeffrey A., Lehner, Bernhard, Carrea, Laura, 2024. LakeTEMP. figshare. Journal contribution. https://doi.org/10.6084/m9.figshare.23844660. [dataset].

Lamaro, A.A., Mariñelarena, A., Torrusio, S.E., Sala, S.E., 2013. Water surface temperature estimation from Landsat 7 ETM+ thermal infrared data using the generalized single-channel method: case study of Embalse del Río Tercero (Córdoba, Argentina). Adv. Space Res. 51 (3), 492–500. https://doi.org/10.1016/j.asr.2012.09.032.

Lead, P.I.N., Magnuson, J., Carpenter, S., Stanley, E., 2020. North Temperate Lakes LTER: High Frequency Water Temperature Data - Trout Lake Buoy 2004 - current ver 26. Environmental Data Initiative. https://doi.org/10.6073/pasta/6ad563f6059685a116754ff3b391d15e [Date accessed: 2021-12-02] [dataset].

Lehner, B., Messager, M.L., Korver, M.C., Linke, S., 2022. Global hydro-environmental lake characteristics at high spatial resolution. Sci. Data 9 (1). https://doi.org/10.1038/s41597-022-01425-z.

Liu, Y., Dworak, R., Key, J., 2018. Ice surface temperature retrieval from a single satellite imager band. Remote Sens. 10 (12) https://doi.org/10.3390/rs10121909.

LSPA, Weathers, K.C., and Steele, B.G, 2021. Lake Sunapee Instrumented Buoy: High Frequency Water Temperature and Dissolved Oxygen Data - 2007-2020 ver 2. Environmental Data Initiative. https://doi.org/10.6073/pasta/0c5298c55a128be56ba57449c795df63 [Date accessed: 2021-12-02] [dataset].

Lucius, M.A., Moriarty, V.W., Kolar, H.R., Eichler, L.W., Corbiere, M.M., Kelly, M.R., Rose, K.C., 2022a. The Jefferson Project 2019 water quality data from three vertical profiler stations in Lake George, NY, USA. ver 1. Environmental Data Initiative. https://doi.org/10.6073/pasta/572fab5d802406269a8ce53e985c4b4a [Date accessed: 2022-05-31] [dataset].

Lucius, M.A., Moriarty, V.W., Kolar, H.R., Eichler, L.W., Corbiere, M.M., Kelly, M.R., Rose, K.C., 2022b. The Jefferson Project 2018 Water Quality Data from Two Vertical Profiler Stations in Lake George, NY, USA. ver 1. Environmental Data Initiative. https://doi.org/10.6073/pasta/52223cea9831631afd537676dd0ae3ef [Date accessed: 2022-05-31] [dataset].

Maberly, S.C., O'Donnell, R.A., Woolway, R.I., Cutler, M.E.J., Gong, M., Jones, I.D., Merchant, C.J., Miller, C.A., Politi, E., Scott, E.M., Thackeray, S.J., Tyler, A.N., 2020. Global lake thermal regions shift under climate change. Nat. Commun. 11 (1), 1232. https://doi.org/10.1038/s41467-020-15108-z.

MacCallum, S.N., Merchant, C.J., 2012. Surface water temperature observations of large lakes by optimal estimation. Can. J. Remote. Sens. 38 (1), 25–45. https://doi.org/10.5589/m12-010.

Magnuson, J.J., Carpenter, S.R., Stanley, E.H., 2023. North Temperate Lakes LTER: High Frequency Water Temperature Data - Lake Mendota Buoy 2006 - Current ver 31. Environmental Data Initiative. https://doi.org/10.6073/pasta/2d6db053cfe03be2ddd3fbc0d86a6fb3 [Date accessed: 2023-01-07] [dataset].

Marszelewski, W., Skowron, R., 2006. Ice cover as an indicator of winter air temperature changes: case study of the polish lowland lakes. Hydrol. Sci. J. 51 (2), 336–349. https://doi.org/10.1623/hysj.51.2.336.

Martinsen, K.T., Andersen, M.R., Sand-Jensen, K., 2019. Water temperature dynamics and the prevalence of daytime stratification in small temperate shallow lakes. Hydrobiologia 826 (1), 247–262. https://doi.org/10.1007/s10750-018-3737-2.

Mason, L.A., Riseng, C.M., Gronewold, A.D., Rutherford, E.S., Wang, J., Clites, A., Smith, S.D.P., McIntyre, P.B., 2016. Fine-scale spatial variation in ice cover and surface temperature trends across the surface of the Laurentian Great Lakes. Clim. Chang. 138 (1), 71–83. https://doi.org/10.1007/s10584-016-1721-2.

McKnight, E., 2022. Limnology of a Large Northern Lake (Lhù'ààn Mân' [Kluane Lake], Yukon) in an Era of Reconciliation and Rapid Climate Change. PhD Thesis. ERA. https://doi.org/10.7939/r3-3ba4-qw40.

Messager, M.L., Lehner, B., Grill, G., Nedeva, I., Schmitt, O., 2016. Estimating the volume and age of water stored in global lakes using a geo-statistical approach. Nat. Commun. 7 (1), 13603. https://doi.org/10.1038/ncomms13603.

Miljödata, M.V.M., 2023. Swedish University of Agricultural Sciences (SLU). National Data Host Lakes and Watercourses, and National Data Host Agricultural Land. https://miljodata.slu.se/mvm/ [Date accessed: 2023-01-07].

Murfitt, J., Duguay, C.R., 2021. 50 years of lake ice research from active microwave remote sensing: Progress and prospects. Remote Sens. Environ. 264, 112616 https://doi.org/10.1016/j.rse.2021.112616.

National Ecological Observatory Network (NEON), 2021. Temperature at Specific Depth in Surface Water. Data Product DP1.20264.001. NEON, Battelle, Boulder, CO, USA. https://data.neonscience.org [Date accessed 2021-11-30] [dataset].

Nonaka, T., Matsunaga, T., Hoyano, A., 2007. Estimating ice breakup dates on Eurasian lakes using water temperature trends and threshold surface temperatures derived from MODIS data. Int. J. Remote Sens. 28 (10), 2163–2179. https://doi.org/10.1080/01431160500391957.

Pekel, J.-F., Cottam, A., Gorelick, N., Belward, A.S., 2016. High-resolution mapping of global surface water and its long-term changes. Nature 540 (7633), 418–422. https://doi.org/10.1038/nature20584.

Pi, X., Luo, Q., Feng, L., Xu, Y., Tang, J., Liang, X., Ma, E., Cheng, R., Fensholt, R., Brandt, M., Cai, X., Gibson, L., Liu, J., Zheng, C., Li, W., Bryan, B.A., 2022. Mapping global lake dynamics reveals the emerging roles of small lakes. Nat. Commun. 13 (1) https://doi.org/10.1038/s41467-022-33239-3.

Ramachandran, R., Bugbee, K., Murphy, K., 2021. From open data to Open Science. Earth and Space Sci. 8 (5) https://doi.org/10.1029/2020EA001562.

Råman Vinnå, L., Wüest, A., Bouffard, D., 2017. Physical effects of thermal pollution in lakes. Water Resour. Res. 53 (5), 3968–3987. https://doi.org/10.1002/2016WR019686.

Sharma, S., Gray, D.K., Read, J.S., O'Reilly, C.M., Schneider, P., Qudrat, A., Gries, C., Stefanoff, S., Hampton, S.E., Hook, S., Lenters, J.D., Livingstone, D.M., McIntyre, P. B., Adrian, R., Allan, M.G., Anneville, O., Arvola, L., Austin, J., Bailey, J., Woo, K.H., 2015. A global database of lake surface temperatures collected by in situ and satellite methods from 1985–2009. Sci. Data 2 (1). https://doi.org/10.1038/sdata.2015.8.

Sharma, S., Blagrave, K., Magnuson, J.J., O'Reilly, C.M., Oliver, S., Batt, R.D., Magee, M. R., Straile, D., Weyhenmeyer, G.A., Winslow, L., Woolway, R.I., 2019. Widespread loss of lake ice around the northern hemisphere in a warming world. Nat. Clim. Chang. 9 (3), 227–231. https://doi.org/10.1038/s41558-018-0393-5.

Sharma, S., Filazzola, A., Nguyen, T., Imrit, M.A., Blagrave, K., Bouffard, D., Daly, J., Feldman, H., Feldsine, N., Hendricks-Franssen, H.-J., Granin, N., Hecock, R., L'Abée-Lund, J.H., Hopkins, E., Howk, N., Iacono, M., Knoll, L.B., Korhonen, J., Malmquist, H.J., Magnuson, J.J., 2022. Long-term ice phenology records spanning up to 578 years for 78 lakes around the northern hemisphere. Sci. Data 9 (1). https://doi.org/10.1038/s41597-022-01391-6.

Simon, R.N., 2014. Retrieving water surface temperature from archive LANDSAT thermal infrared data: application of the mono-channel atmospheric correction algorithm over two freshwater reservoirs. Int. J. Appl. Earth Obs. Geoinf. 30, 247–250. https://doi.org/10.1016/j.jag.2014.01.005.

Striegl, R.G., Kortelainen, P., Chanton, J.P., Wickland, K.P., Bugna, G.C., Rantakari, M., 2001. Carbon dioxide partial pressure and 13C content of north temperate and boreal lakes at spring ice melt. Limnol. Oceanogr. 46 (4), 941–945. https://doi.org/10.4319/lo.2001.46.4.0941.

Sunday, J.M., Bates, A.E., Dulvy, N.K., 2012. Thermal tolerance and the global redistribution of animals. Nat. Clim. Chang. 2 (9) https://doi.org/10.1038/nclimate1539.

Tong, Y., Feng, L., Wang, X., Pi, X., Xu, W., Woolway, R.I., 2023. Global lakes are warming slower than surface air temperature due to accelerated evaporation. Nature Water 1 (11), 929–940. https://doi.org/10.1038/s44221-023-00148-8.

United States Geological Survey, 2021. Landsat 8 Collection 1 Tier 1 TOA Reflectance. Accessed from Google Earth Engine between August 9 – August 21, 2021 [dataset].

Vachon, D., Sponseller, R.A., Karlsson, J., 2021. Integrating carbon emission, accumulation and transport in inland waters to understand their role in the global carbon cycle. Glob. Chang. Biol. 27 (4), 719–727. https://doi.org/10.1111/gcb.15448.

von Storch, H., Zwiers, F.W., 1999. Statistical Analysis in Climate Research. Cambridge University Press, p. 484. https://doi.org/10.1017/CBO9780511612336.

Wang, X., Qiu, Y., Zhang, Y., Lemmetyinen, J., Cheng, B., Liang, W., Leppäranta, M., 2022. A lake ice phenology dataset for the northern hemisphere based on passive microwave remote sensing. Big. Earth Data 6 (4), 401–419. https://doi.org/10.1080/20964471.2021.1992916.

Willard, J.D., Read, J.S., Topp, S., Hansen, G.J.A., Kumar, V., 2022. Daily surface temperatures for 185,549 lakes in the conterminous United States estimated using deep learning (1980–2020). Limnol. Oceanography Lett. 7 (4), 287–301. https://doi.org/10.1002/lol2.10249.

Wilson, R.C., Hook, S.J., Schneider, P., Schladow, S.G., 2013. Skin and bulk temperature difference at Lake Tahoe: A case study on lake skin effect. J. Geophys. Res. Atmos. 118, 10,332–10,346. https://doi.org/10.1002/jgrd.50786.

Winslow, L.A., Read, J.S., Hansen, G.J.A., Hanson, P.C., 2015. Small lakes show muted climate change signal in Deepwater temperatures. Geophys. Res. Lett. 42 (2), 355–361. https://doi.org/10.1002/2014GL062325.

Wloczyk, C., Richter, R., Borg, E., Neubert, W., 2006. Sea and lake surface temperature retrieval from Landsat thermal data in northern Germany. Int. J. Remote Sens. 27 (12), 2489–2502. https://doi.org/10.1080/01431160500300206.

Wood, S., 2017. Generalized Additive Models: An Introduction with R, 2nd edition. Chapman and Hall/CRC.

Woodward, G., Perkins, D.M., Brown, L.E., 2010. Climate change and freshwater ecosystems: impacts across multiple levels of organization. Philosoph. Trans. Royal Soc., B: Biol. Sci. 365 (1549), 2093–2106. https://doi.org/10.1098/rstb.2010.0055.

Woolway, R.I., Merchant, C.J., 2018. Intralake heterogeneity of thermal responses to climate change: A study of large northern Hemisphere Lakes. J. Geophys. Res. Atmos. 123 (6), 3087–3098. https://doi.org/10.1002/2017JD027661.

Woolway, R.I., Merchant, C.J., 2019. Worldwide alteration of lake mixing regimes in response to climate change. Nat. Geosci. 12 (4), 271–276. https://doi.org/10.1038/s41561-019-0322-x.

Woolway, R.I., Jennings, E., Shatwell, T., Golub, M., Pierson, D.C., Maberly, S.C., 2021. Lake heatwaves under climate change. Nature 589, 402–407. https://doi.org/10.1038/s41586-020-03119-1.

Woolway, R.I., Maberly, S.C., Jones, I.D., Feuchtmayr, H., 2014. A novel method for estimating the onset of thermal stratification in lakes from surface water measurements. Water Resour. Res. 50 (6), 5131–5140. https://doi.org/10.1002/2013WR014975.

Woolway, R.I., Verburg, P., Merchant, C.J., Lenters, J.D., Hamilton, D.P., Brookes, J., Kelly, S., Hook, S., Laas, A., Pierson, D., Rimmer, A., Rusak, J.A., Jones, I.D., 2017. Latitude and lake size are important predictors of over-lake atmospheric stability. Geophys. Res. Lett. 44 (17), 8875–8883. https://doi.org/10.1002/2017GL073941.

Woolway, R.I., Albergel, C., Frölicher, T.L., Perroud, M., 2022. Severe Lake heatwaves attributable to human-induced global warming. Geophys. Res. Lett. 49 (4) https://doi.org/10.1029/2021GL097031.

Yang, B., Wells, M.G., McMeans, B.C., Dugan, H.A., Rusak, J.A., Weyhenmeyer, G.A., Brentrup, J.A., Hrycik, A.R., Laas, A., Pilla, R.M., Austin, J.A., Blanchfield, P.J., Carey, C.C., Guzzo, M.M., Lottig, N.R., MacKay, M.D., Middel, T.A., Pierson, D.C., Wang, J., Young, J.D., 2021. A new thermal categorization of ice-Covered Lakes. Geophys. Res. Lett. 48 (3) https://doi.org/10.1029/2020GL091374.

Zhang, X., Wang, K., Kirillin, G., 2021. An automatic method to detect Lake ice phenology using MODIS daily temperature imagery. Remote Sens. 13 (14) https://doi.org/10.3390/rs13142711.

Zhao, G., Li, Y., Zhou, L., Gao, H., 2022. Evaporative water loss of 1.42 million global lakes. Nat. Commun. 13 (1) https://doi.org/10.1038/s41467-022-31125-6.